Science Advances
AAAS

Supplementary Materials for

Dynamic phase transitions dictate the size effect and activity of supported gold catalysts

Lei Zhou *et al.*

Corresponding author: Jin-Cheng Liu, liujincheng@nankai.edu.cn; Jun Li, junli@tsinghua.edu.cn; Chun-Jiang Jia, jiacj@sdu.edu.cn; Yang He, yanghe@ustb.edu.cn

Sci. Adv. **10**, eadr4145 (2024)
DOI: 10.1126/sciadv.adr4145

The PDF file includes:

Other Supplementary Material for this manuscript includes the following:

Supplementary Text

Functional test

In this study, we considered the PBE, PBE + D3, PBE + D3BJ, PBEsol, revPBE, RPBE, and SCAN + rVV10 functionals and compared their performance in describing the (i) lattice constants of optimized crystal structure, (ii) CO adsorption enthalpies on Au surfaces, and (iii) surface reconstruction (**fig. S6**). The results are as follows:

(i) Our results showed that PBE + D3, PBE + D3BJ, PBEsol, and SCAN + rVV10 were effective in describing the Au bulk lattice parameters and surface structures, while PBE, revPBE and RPBE overestimated the lattice parameters by approximately 2%, a common phenomenon for GGA functionals.

(ii) The experimental adsorption enthalpies of CO on Au(100), Au(110)-*p*(1×2), and Au(332) surfaces are about −0.55 eV, −0.47 eV, and −0.57 eV, respectively. The PBE + D3, PBE + D3BJ, PBEsol and SCAN + rVV10 overestimated the adsorption enthalpies by approximately −0.30~−0.40 eV, while revPBE and RPBE underestimated the adsorption enthalpies. In contrast, only PBE could accurately describe the CO adsorption enthalpy on Au surfaces.

(iii) Additionally, LEED results indicated a well-known surface missing row reconstruction of Au(110)-*p*(1×2) with a significant contraction of −0.25 Å. PBE + D3, revPBE, RPBE, and SCAN + rVV10 failed to describe the surface redistribution of the Au(110) surface, while PBE, PBE + D3BJ and PBEsol were effective in describing this phenomenon. Based on our test, only the PBE functional could accurately describe both the surface redistribution and CO adsorption enthalpy, simultaneously. Therefore, we adopted the PBE functional for all DFT calculations in this work.

Post processing of molecular dynamics

Molecular dynamics simulations generate vast amounts of data that require post-processing to extract useful information about the system being studied. One commonly used post-processing technique is the calculation of the mean squared displacement (MSD) from the trajectories of individual atoms, which can be used to determine the diffusivity (*D*) of the system. In this study, we used the MDAnalysis package to calculate the MSD according to the Einstein equation for every step (**figs. S8 to S11**).

$$\mathrm{MSD}(\Delta t) = \frac{1}{N}\sum_{i=1}^{N}\frac{1}{N_{\Delta t}}\sum_{t=0}^{t_{tot}-\Delta t}|\boldsymbol{r}_i(t+\Delta t) - \boldsymbol{r}_i(t)|^2 \quad \text{(S1)}$$

where N is the number of Au atoms, t_{tot} is the total simulation time, Δt is the time step, and $\boldsymbol{r}_{\mathrm{i}}(t)$ represents the trajectory of Au atoms at the frame corresponding to simulation time t. The diffusivity of Au is calculated as the slope of the MSD over a time interval Δt according to the Einstein relation:

$$D = \frac{\mathrm{MSD}(\Delta t)}{2d\Delta t} \quad \text{(S2)}$$

where $d = 3$ is the dimension of the 3D system.

Furthermore, the RDF analysis revealed that low-coordinated Au atoms are stabilized by Au-C bonds, which remain largely intact during DPMD simulations. This is evidenced by the minimal density observed between the first and second peaks of the *g*(Au-C) RDF, indicating a strong bond between Au and C. On the other hand, the *g*(Au-Au) RDF shows significant density between the

first and second peaks, indicating that Au-Au bonds are more flexible and can move freely under real catalytic conditions (**fig. S5**). RDFs are also adopted to evaluate the disordering of Au NPs with various sizes under different temperatures (**figs. S12 to S15**).
The Lindemann Index for each atom and the entire system at different temperature are given as:

$$\langle q_i \rangle_{\text{atoms}} = \frac{1}{N(N-1)} \sum_{j \neq i} \frac{\sqrt{\langle r_{ij}{}^2 \rangle - \langle r_{ij} \rangle^2}}{\langle r_{ij} \rangle} \quad \text{(S3)}$$

where N is the number of Au atoms in the simulation system, and r_{ij} is the distance between Au atoms i and j. The angle bracket represents a time average (**figs. S17 to S20**). This index is used to assess the degree of structural disorder and melting in the system. The Lindemann Index is calculated as the ratio of the root-mean-square deviation of the interatomic distances to the mean distance.

Thermodynamics analysis of surface tension

The surface tension of solid gold NPs can be determined by averaging the surface energies using the Curie-Wulff relationship. This relationship demonstrates that the distance of each facet of the NP (d_i) is proportional to the surface tension of the respective (*hkl*) surface.

By applying this relationship, the surface tensions of the (*hkl*) surfaces of the Au NPs (γ_s) can be calculated as an average of the surface tension of each surface:

$$\gamma_s = \sum_i f_i \times \gamma_i \quad \text{(S4)}$$

Based on DFT calculations, the γ_i can be obtained by:

$$\gamma_i = \frac{E_{\text{slab}} - N E_{\text{bulk}}}{2A_i} \quad \text{(S5)}$$

where N is the number of atoms in the slab model, E_{slab} is the total energy of the slab, E_{bulk} is the energy per atom in bulk Au and A_i is the area parallel to surface i. All atoms in the slab model are allowed to relax, while the slab thickness is chosen iteratively for each (*hkl*) model until the surface tension converges within 0.02 J/m^2.

The (*hkl*) planes with high surface tension (usually high-indexed ones) will be drawn at greater distances and are therefore less likely to appear in the equilibrium shape. Therefore, we only considered the *h*, *k*, and *l* index up to 3, based on previously reported work. All the computational surface tensions are listed in **table S1** and closely align with previously reported results. We used the open-source Pymatgen suite to construct and estimate the average surface tension of solid Au NP. The calculated surface tension (γ_s) of bare Au NPs was found to be 0.757 J/m^2, which is lower than the experimental value of 1.38 J/m^2. To account for this discrepancy, a scaling factor of 1.824 was applied to the calculated surface tension in this work. For further thermodynamic analysis, the experimental liquid Au surface tension of 1.135 J/m^2 was adopted.

In order to study the adsorption of CO on solid Au NPs' surfaces, the adsorption energies of CO molecules on Au(*hkl*) surfaces were calculated. These adsorption energies are shown in a table with CO coverage (θ) equal to 1/4, 1/2, 3/4, and 1. As shown in **table S2 and fig. S21**, the adsorption energy, $E_{CO}^{ads}(\theta_i)$, typically shows a linear correlation with the CO coverage, θ_i,

$$E_{CO}^{ads}(\theta_i) = b + a \times \theta_i \quad \text{(S6)}$$

where the a and b are the slope and intercept of the linear fitting, respectively.

It is important to consider that the adsorption of CO on liquid Au surfaces is much stronger than that on solid Au due to the low coordination of Au atoms. To estimate the trend of CO adsorption on liquid Au, we constructed an amorphous Au_{38} cluster, designed to mimic the typical

local structure of liquid-phase Au NP surfaces observed in our DPMD simulations. The adsorption of CO on this surface model is also summarized in **table S2**.

Based on the calculated CO adsorption energies, the differential adsorption energies of CO, $E_{\mathrm{CO}}^{\mathrm{diff}}(\theta_i)$, can be written as,

$$E_{\mathrm{CO}}^{\mathrm{diff}}(\theta_i) = \frac{d\left[\theta_i \times E_{\mathrm{CO}}^{\mathrm{ads}}(\theta_i)\right]}{d\theta_i} = 2a\theta_i + b = \mu_{CO}(T,P) \quad \text{(S7)}$$

The $E_{\mathrm{CO}}^{\mathrm{diff}}(\theta_i)$ should equal the CO chemical potential, $\mu_{\mathrm{CO}}(T, P)$, at a given temperature (T) and pressure (P). $\mu_{\mathrm{CO}}(T, P)$ is the chemical potential of CO molecules in the gas phase, concerning the reference state at T = 0 K. The value of $\mu_{\mathrm{CO}}(T, P)$ can be obtained from JANAF-NIST standard thermodynamic tables (**table S4**),

$$\mu_{CO}(T,P) = \mu_{CO}(T,P^{\emptyset}) + \mathrm{k}T\ln\left(\frac{P}{P^{\emptyset}}\right) \quad \text{(S8)}$$

Thus, the corresponding coverage θ_i of Au surfaces i can be written as:

$$\theta_i = \frac{\mu_{CO}(T,P) - b}{2a} \quad \text{(S9)}$$

The change of γ_s and γ_i with CO adsorption is labeled as $\Delta\gamma_s(T, P)$ and $\Delta\gamma_i(T, P)$, which is a function of T and P. Based on our previously reported method, $\Delta\gamma_i$ is a function of the chemical potential of CO, $\mu_{\mathrm{CO}}(T, P)$.

$$\Delta\gamma_i(T,P) = \frac{\theta_i\left[E_{\mathrm{CO}}^{\mathrm{ads}}(\theta_i) - \mu_{\mathrm{CO}}(T,P)\right]}{A_i} \quad \text{(S10)}$$

where $\Delta\gamma_i(T, P)$ is the change in surface tension of solid Au surface i with CO adsorption at give T and P, A_i is the unit surface area. Based on the above equations,

$$\Delta\gamma_i(T,P) = -\frac{\mu_{CO}(T,P)^2}{4aA_i} + \frac{b\mu_{CO}(T,P)}{2aA_i} - \frac{b^2}{4aA_i} \quad \text{(S11)}$$

All the $\Delta\gamma_i(T, P)$ are summarized in **tables S5 and S6**. By adding those $\Delta\gamma_i$ to γ_i, one can obtain the surface tension of solid Au NP surfaces at different $\mu_{\mathrm{CO}}(T, P)$. Then the Wulff construction and the averaged surface tension can be obtained as listed in **table S7**.

CO oxidation pathways

Supported Au/CeO_2 catalysts exhibit three potential reaction pathways for CO oxidation, namely Mars-van Krevelen (M-vK), Eley-Rideal (E-R), and Langmuir-Hinshelwood (L-H) mechanisms. Among these, the M-vK mechanism is facilitated by surface oxygen on ceria and occurs at the interface between Au and CeO_2. This mechanism can be divided into seven steps:

(1) * + CO(g) → *CO

(2) *CO + $^{\#}$O → *COO$^{\#}$

(3) *COO$^{\#}$ → * + $^{\#}$(Ov) + CO_2(g)

(4) $^{\#}$(Ov) + O_2(g) → $^{\#}O_2$

(5) $^{\#}O_2$ + * + CO(g) → $^{\#}O_2$ +*CO

(6) *CO + $^{\#}O_2$ → *COOO$^{\#}$

(7) *COOO$^{\#}$ → * + $^{\#}$O+ CO_2(g)

where * is bare Au site, and $^{\#}$O is surface lattice oxygen on CeO_2 surface, $^{\#}$(Ov) is the oxygen vacancy.

On Au NPs or clusters, CO oxidation usually adopts the associative or dissociative L-H mechanism. The dissociative L-H mechanism can be divided into four elementary reactions,

(1) * + CO(g) → *CO

(2) * + O_2(g) → *O_2

(3) *O_2 + * → *2O

(4) *CO + *O → 2* + CO_2(g)

The associative L-H mechanism requires a direct connection between adsorbed *O_2 species and adsorbed *CO molecule to *OCOO.

(1) * + CO(g) → *CO

(2) * + O_2(g) → *O_2

(3) *CO + *O_2 → *OCOO + *

(4) *OCOO → *O + CO_2(g)

(5) *CO + *O → 2* + CO_2(g)

First, the L-H mechanism is calculated for large Au NPs, considering the Au(111), Au(100), Au(211), Au(221), Au(311), and Au(321) surfaces (**table S8** and **figs. S23 to S28**). These surfaces are identified as the most exposed surfaces based on Wulff construction estimation (**fig. S22**). Then, the L-H mechanism is also calculated for supported Au_{12} clusters on the CeO_2(111) surface (**table S9** and **fig. S29**). Last, the M-vK mechanism is calculated for supported Au_{12} clusters on the CeO_2 surface (**table S10** and **fig. S30**).

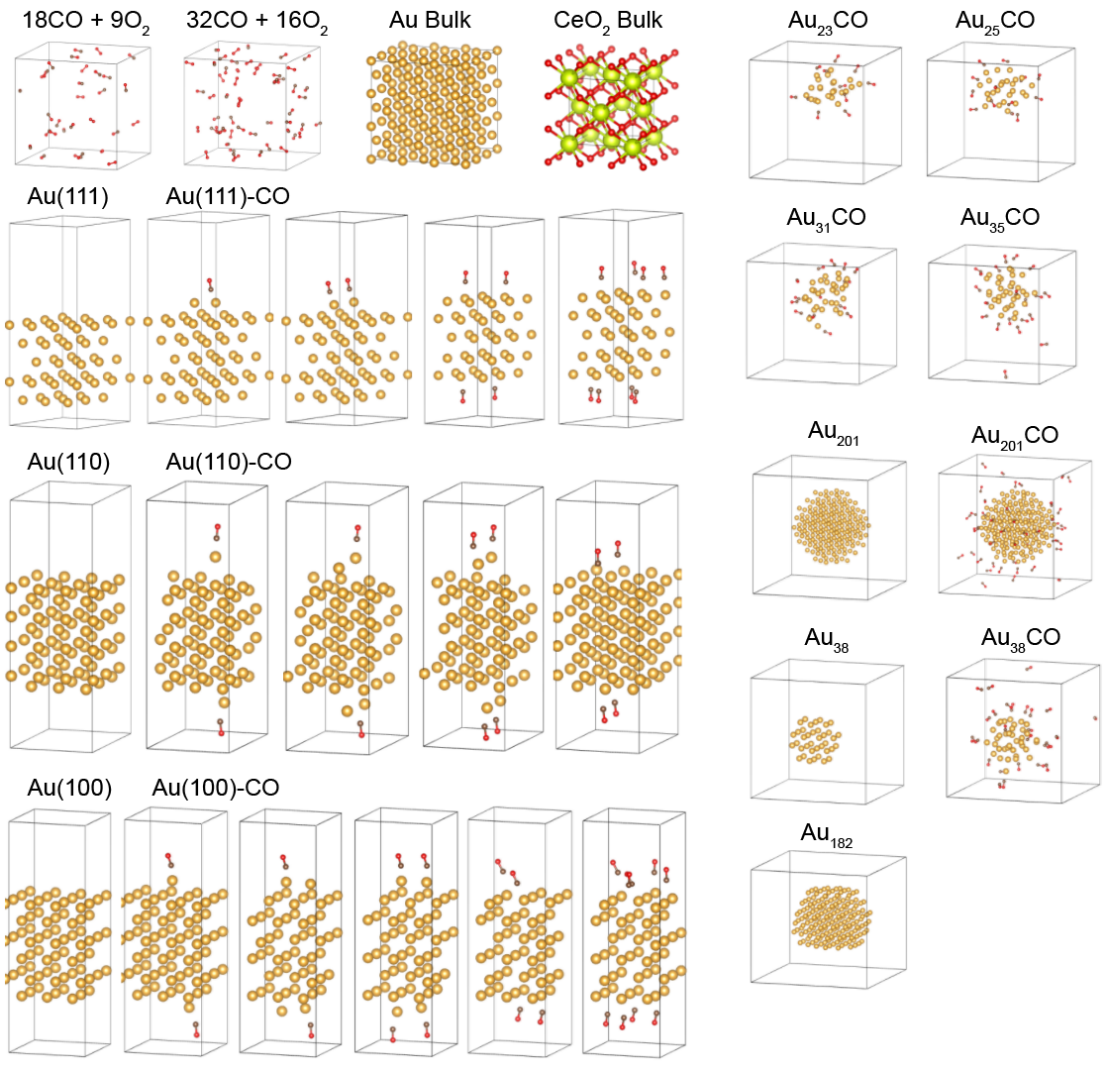

Fig. S1.

Part of the initial structures used for AIMD simulations, whose trajectories are adopted for DeePMD-kit training.

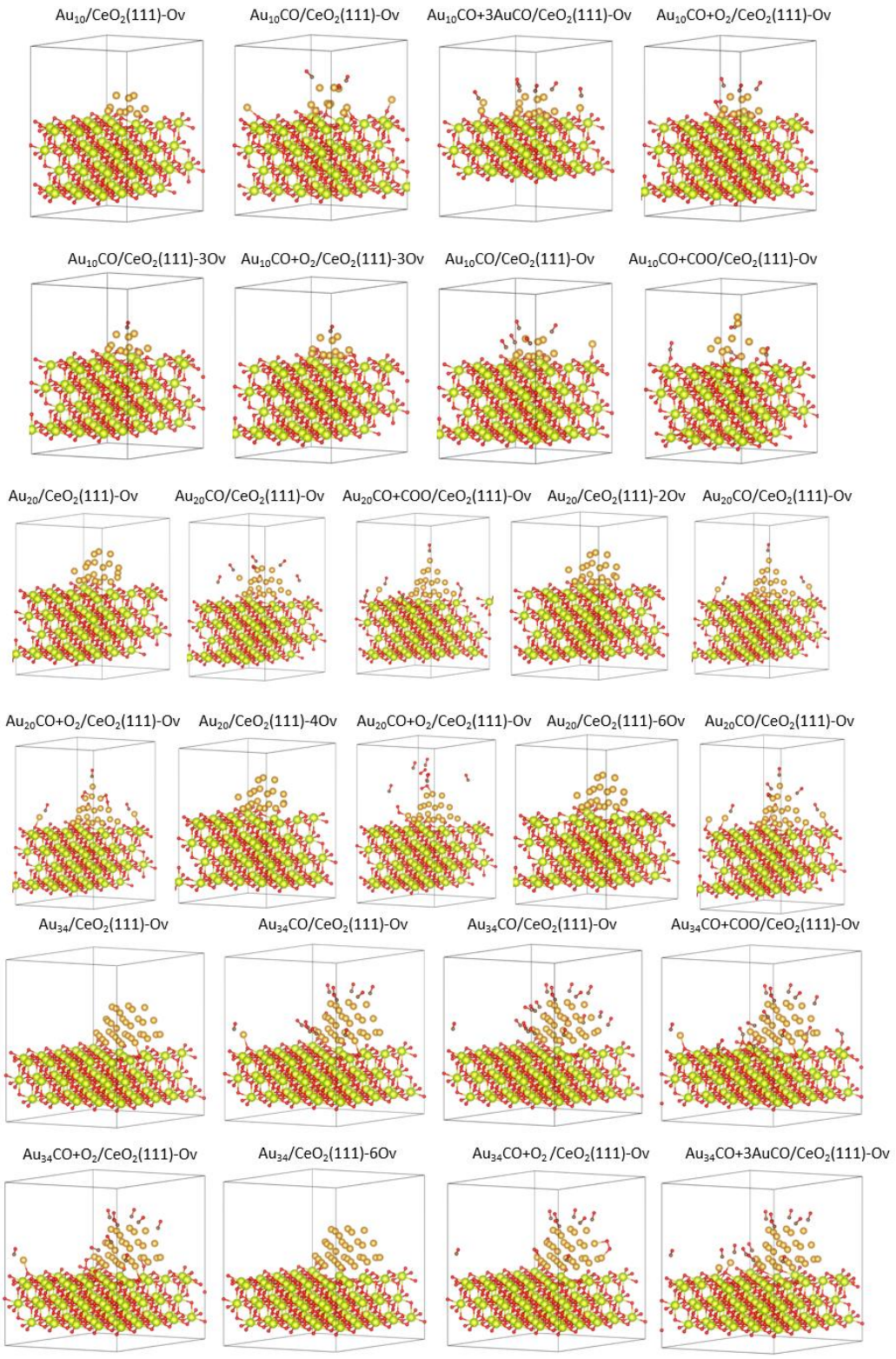

Fig. S2.

Part of the initial structures used for AIMD simulations, whose trajectories are adopted for DeePMD-kit training.

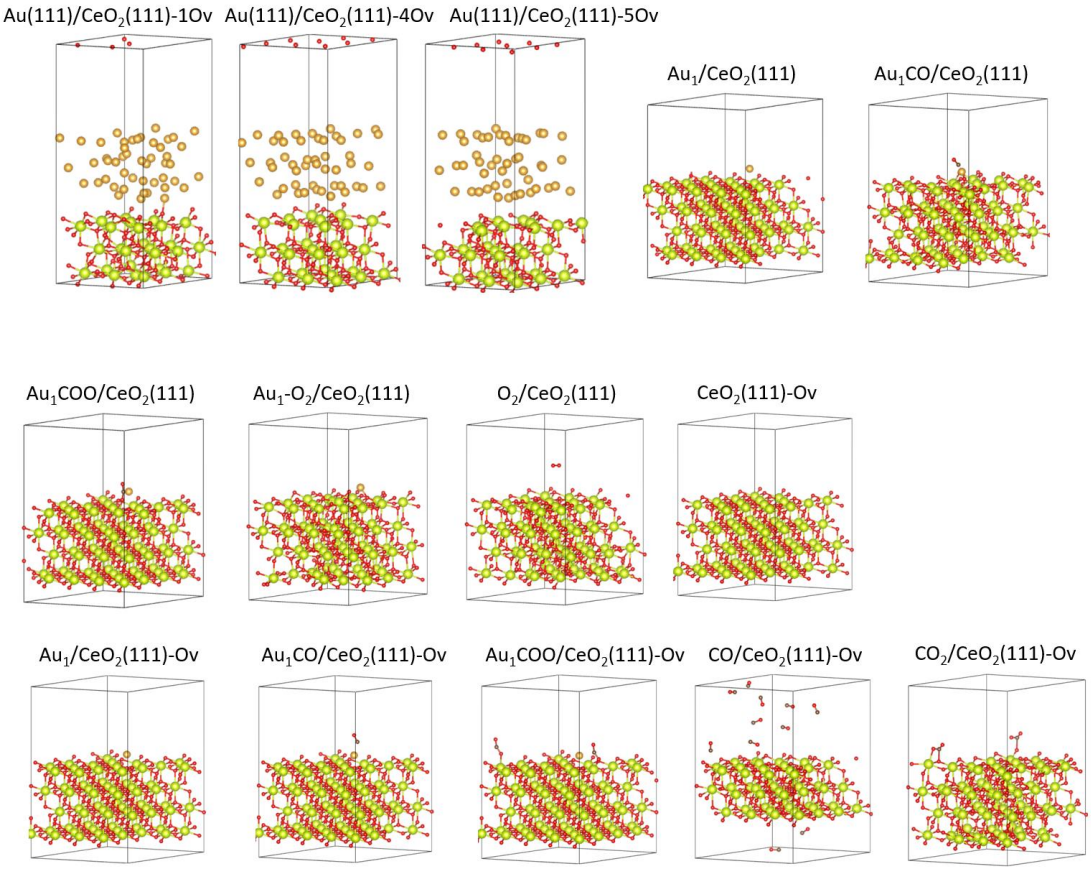

Fig. S3.

Part of the initial structures used for AIMD simulations, whose trajectories are adopted for DeePMD-kit training.

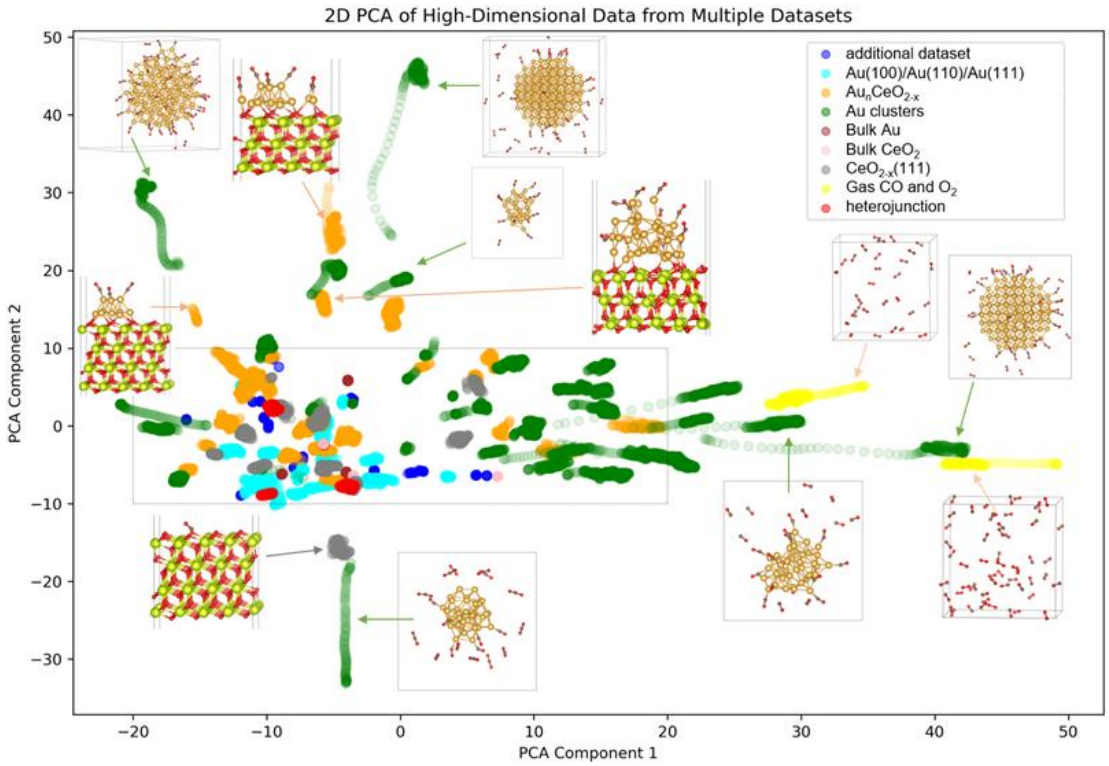

Fig. S4.

A similarity map of training set of local environments embedding net is obtained by PCA.

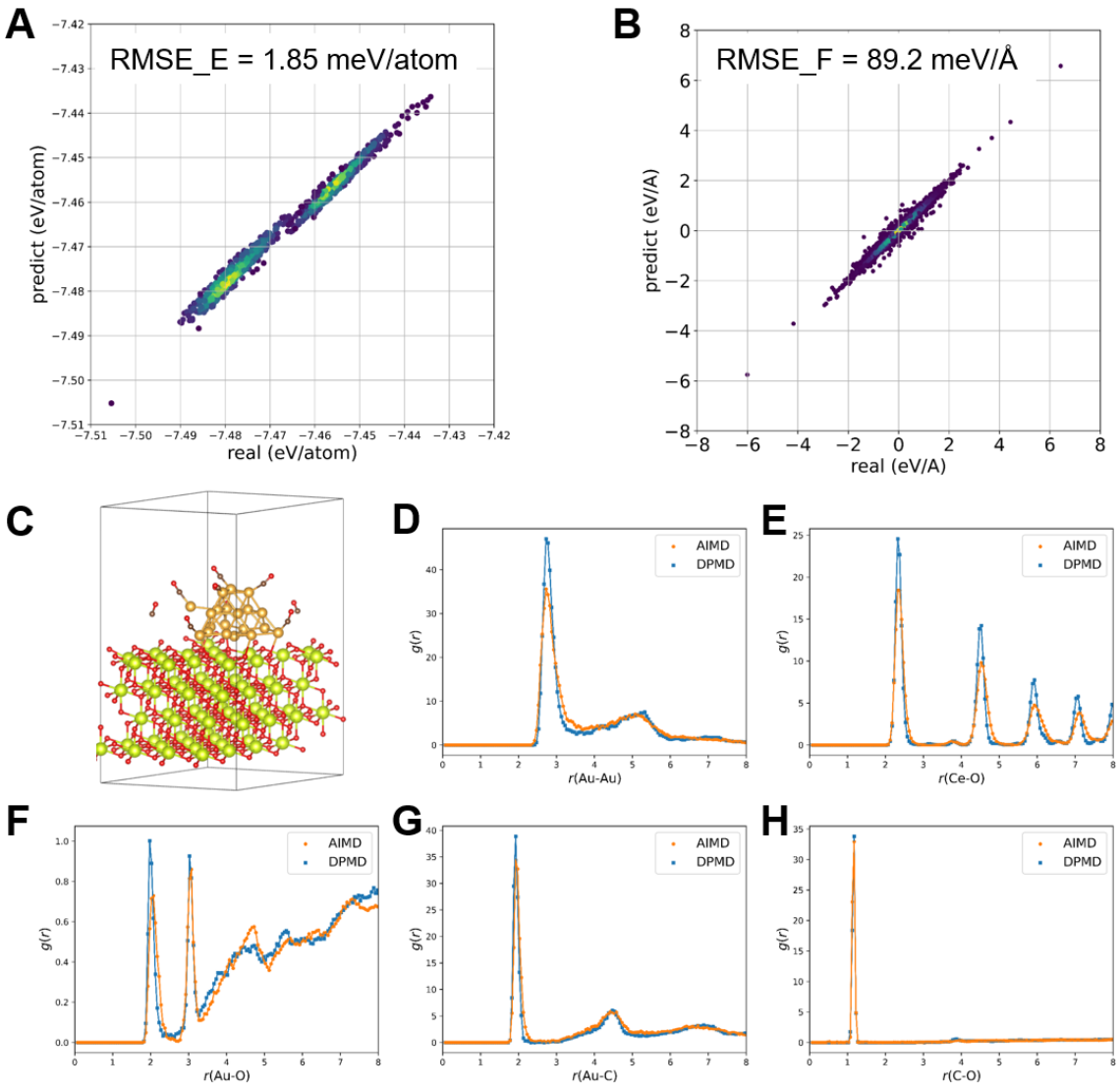

Fig. S5.

Comparison between DFT and deep potential and radius distribution functions (RDFs) of $Au_{20}CO/CeO_2$-$2O_v$. Comparison of energies (A) and forces (B) over a data set that was included in the training. Initial structures (C) for the AIMD and DPMD comparison. RDF of (D) Au-Au, (E) Ce-O, (F) Au-O, (G) Au-C, and (H) C-O of $Au_{20}CO/CeO_2$-$2O_v$ from AIMD and DPMD simulations at 500 K.

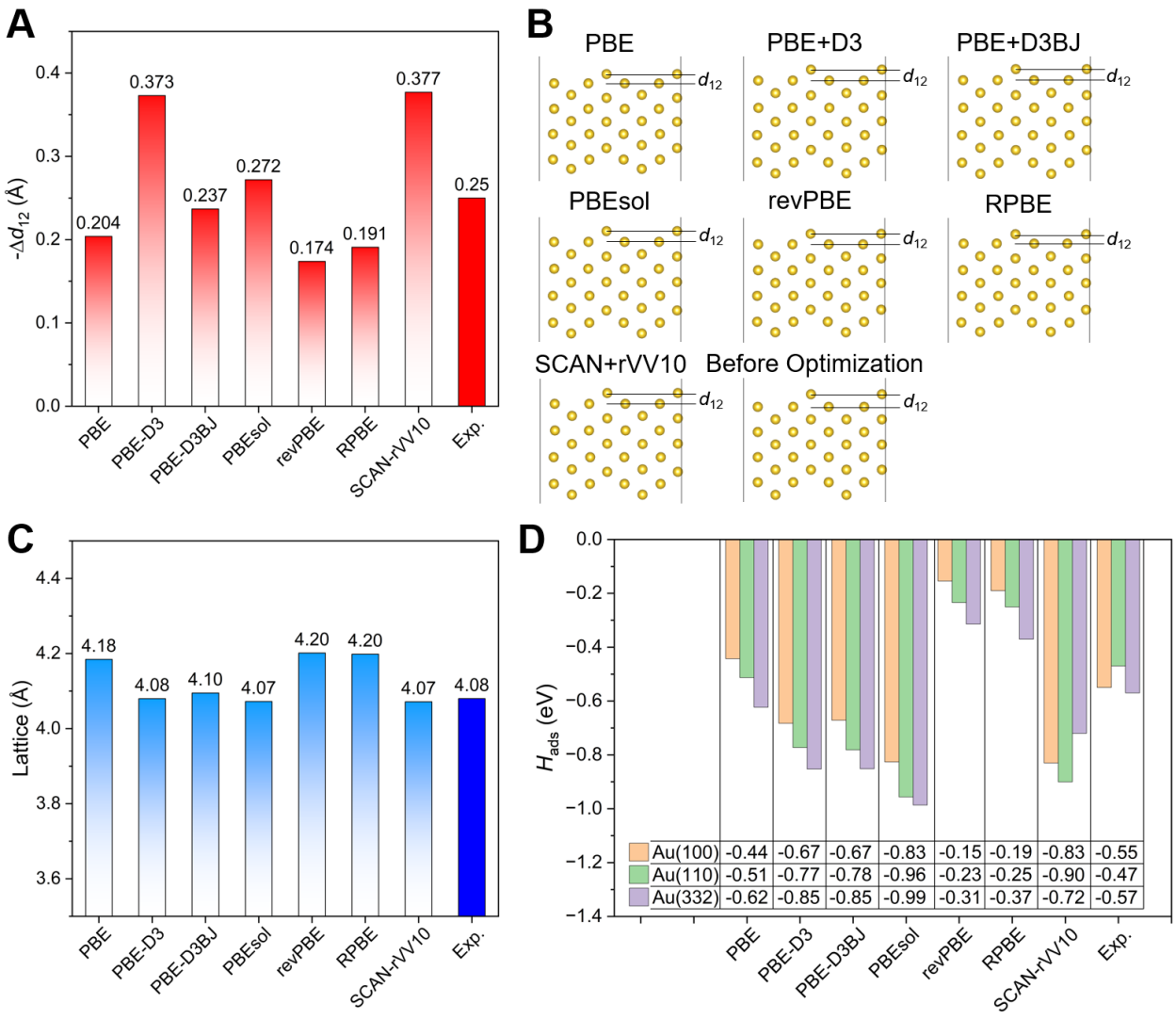

Fig. S6.

Comparisons of PBE, PBE+D3, PBE+D3BJ, PBEsol, revPBE, RPBE, and SCAN+rVV10 functionals with experimental data. (A) The atomic displacements (in Å) between the first and second layers (Δd_{12}) in the Au(110)-p(1×2) surface and (B) the corresponding optimized structures. The experimental data of Δd_{12} = −0.25 Å is measured by scattering and recoiling imaging spectrometry (SARIS) technique. (C) Au bulk lattice parameters. (D) The experimentally measured adsorption enthalpy of CO (H_{ads}) on Au(100), Au(110)-p(1×2), and Au(332) surface and the calculated values by different functionals.

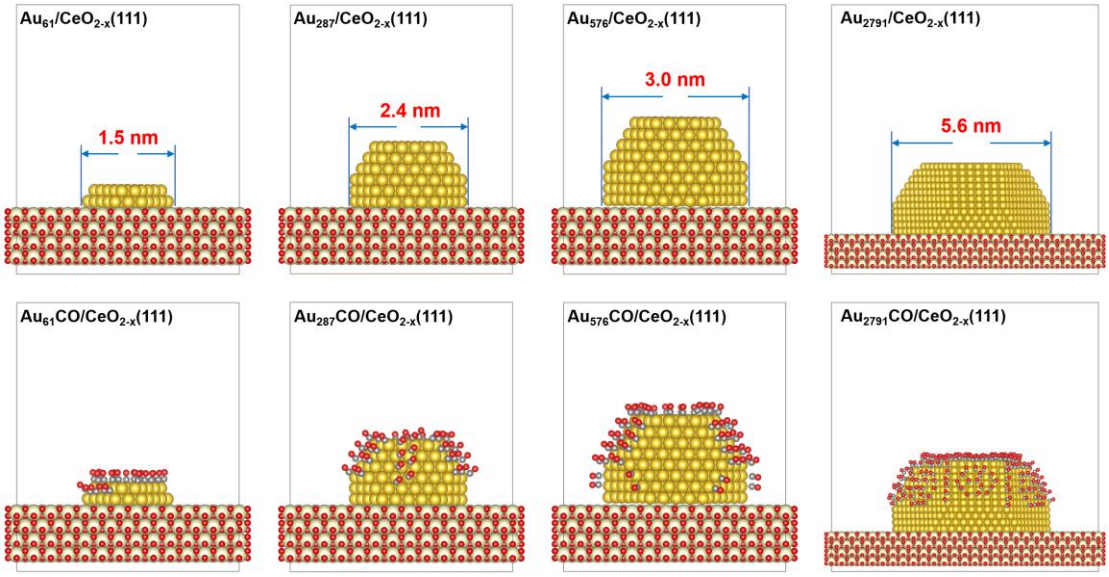

Fig. S7.

Initial configuration of $Au_{61}/CeO_{2-x}(111)$, $Au_{287}/CeO_{2-x}(111)$, $Au_{576}/CeO_{2-x}(111)$ and $Au_{2791}/CeO_{2-x}(111)$ without and with CO molecules.

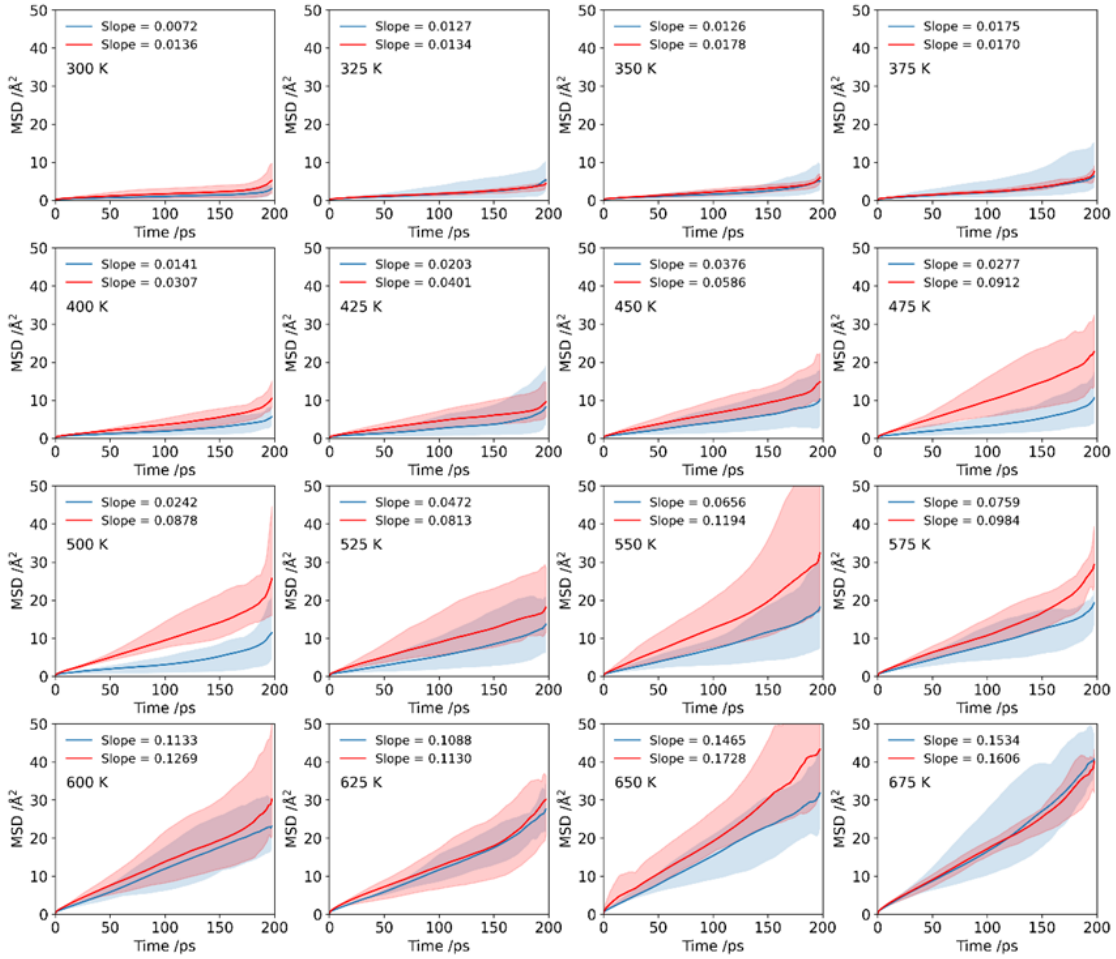

Fig. S8.

Mean square displacements (MSD) averaged over 5 DPMD simulations trajectories for Au_{61}/CeO_{2-x} and $Au_{61}CO/CeO_{2-x}$ from 300 K to 675 K, and their corresponding slopes (*S*) in a unit of $Å^2/ps$.

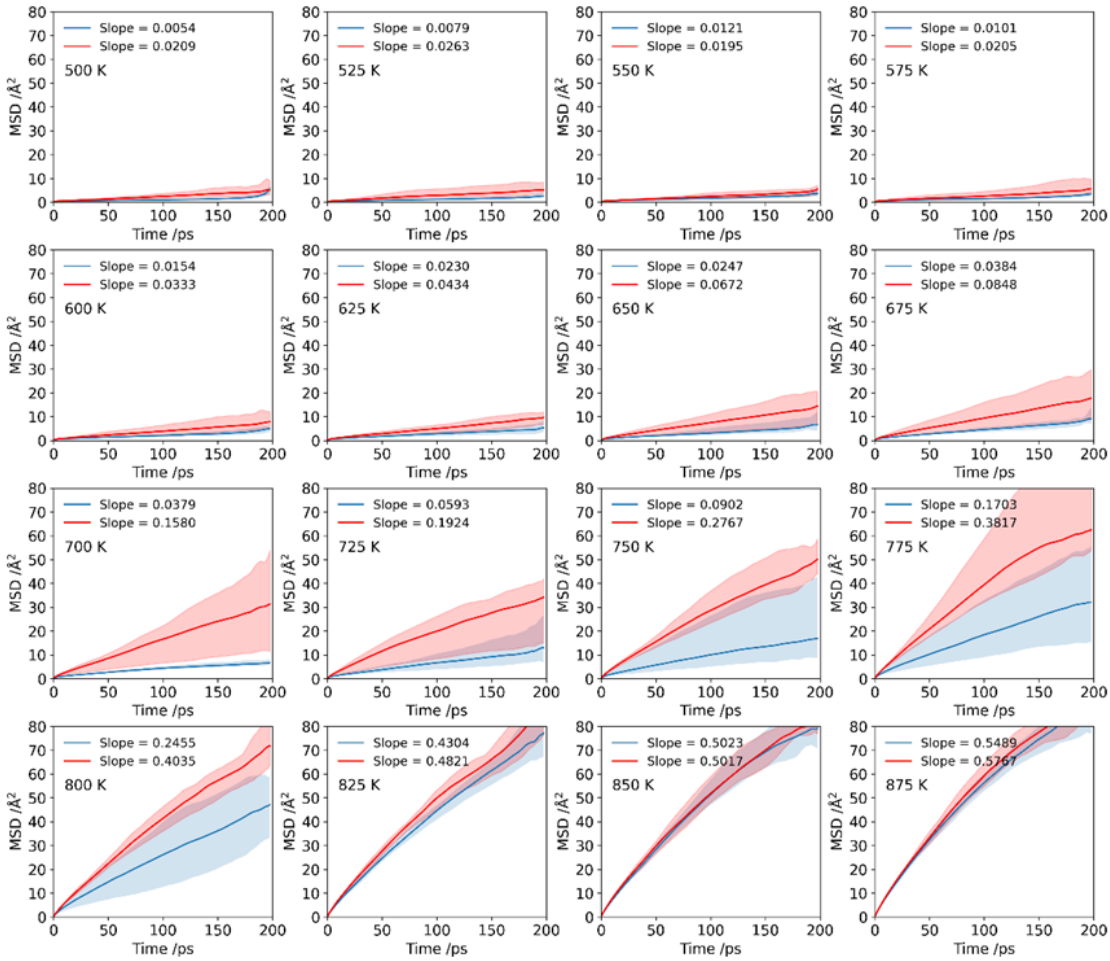

Fig. S9.

Mean square displacements (MSD) averaged over 5 DPMD simulations trajectories for Au_{287}/CeO_{2-x} and $Au_{287}CO/CeO_{2-x}$ from 500 K to 875 K, and their corresponding slopes (*S*) in a unit of $Å^2/ps$.

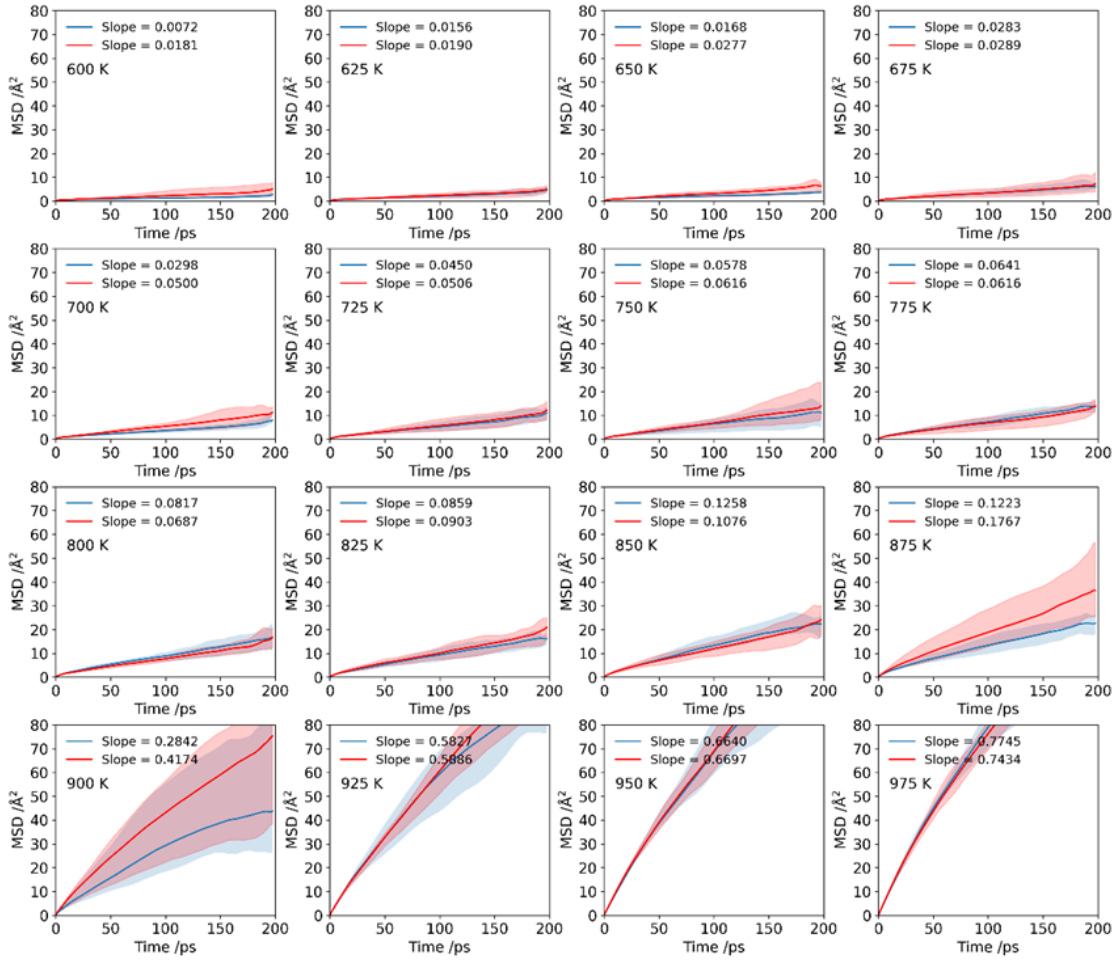

Fig. S10.

Mean square displacements (MSD) averaged over 5 DPMD simulations trajectories for Au_{576}/CeO_{2-x} and $Au_{576}CO/CeO_{2-x}$ from 600 K to 975 K, and their corresponding slopes (*S*) in a unit of $Å^2/ps$.

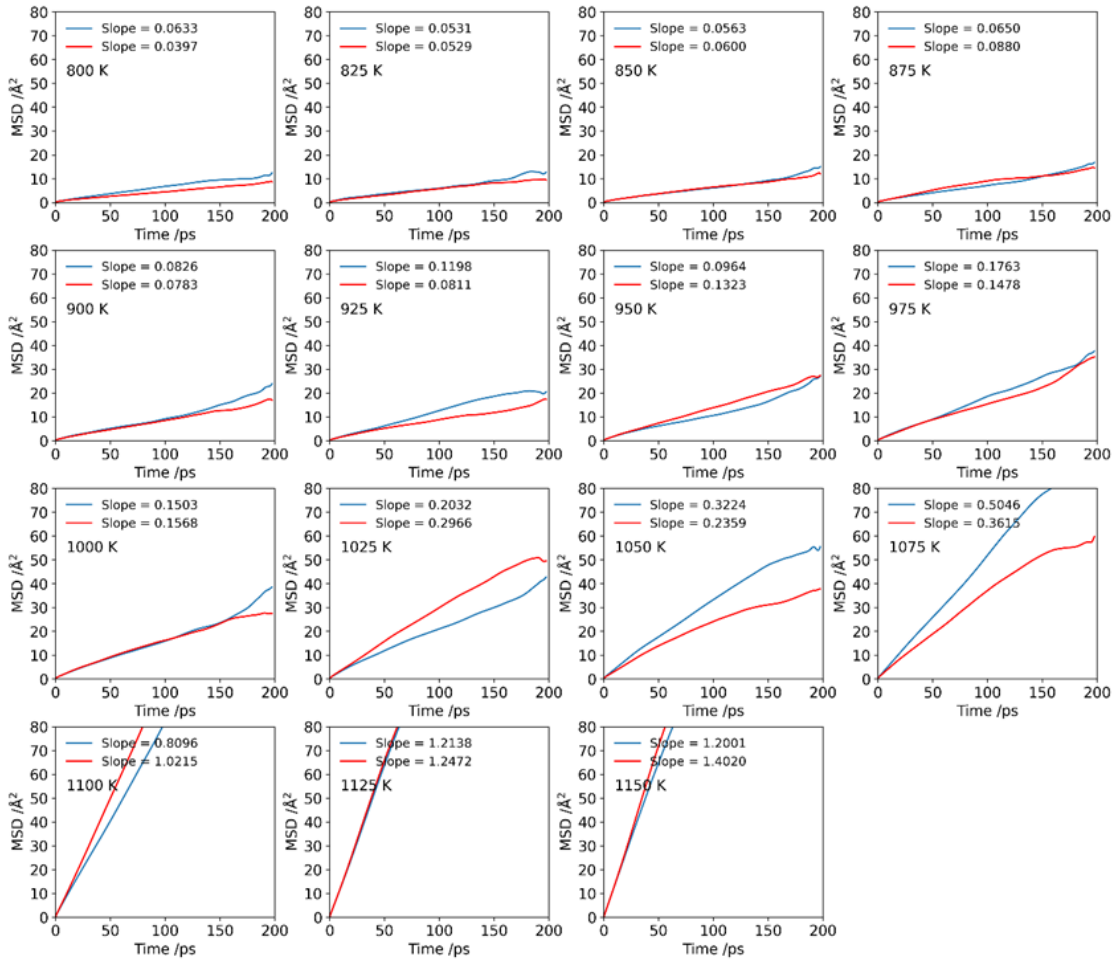

Fig. S11.

Mean square displacements (MSD) of 1 DPMD simulations trajectory for Au_{2791}/CeO_{2-x} and $Au_{2791}CO/CeO_{2-x}$ from 800 K to 1150 K, and their corresponding slopes (*S*) in a unit of $Å^2$/ps.

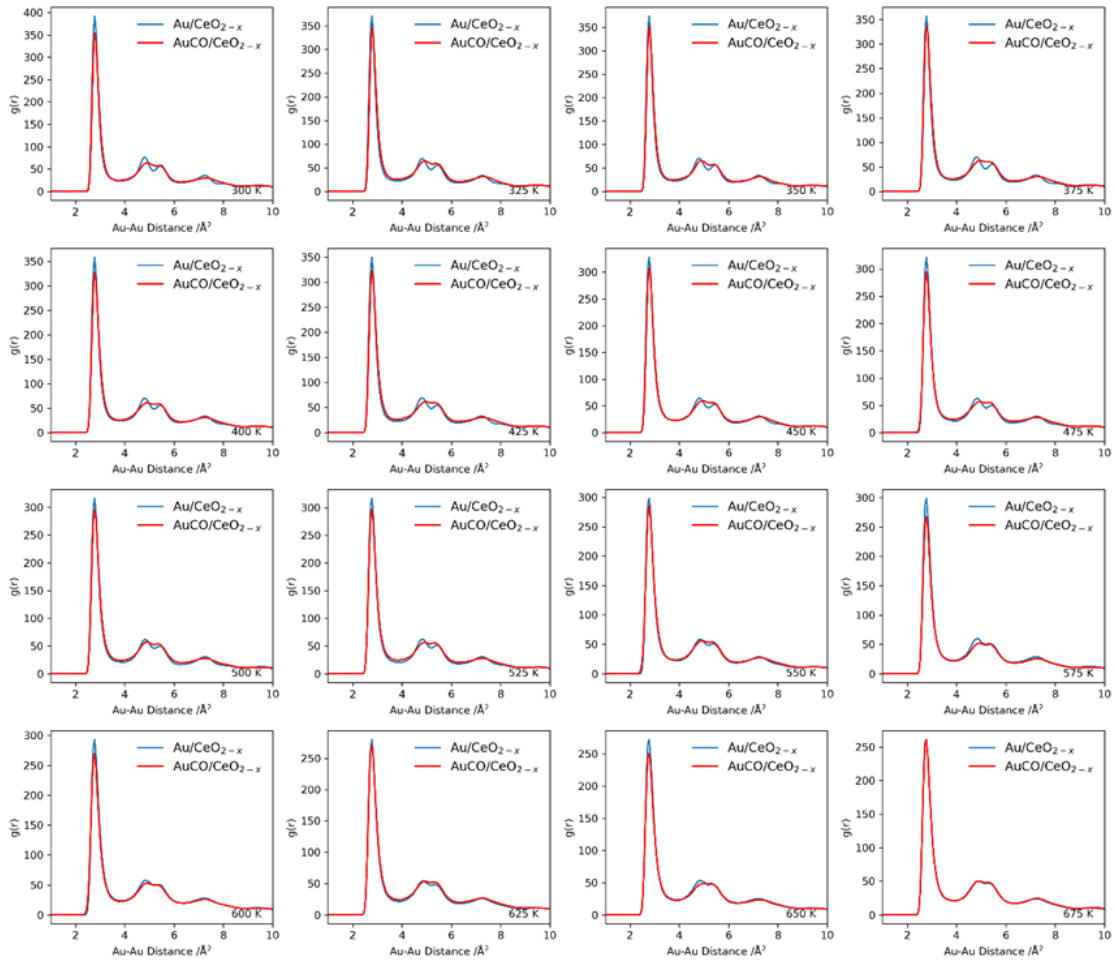

Fig. S12.

RDF of Au-Au pair for Au_{61}/CeO_{2-x} and $Au_{61}CO/CeO_{2-x}$ from 300 K to 675 K.

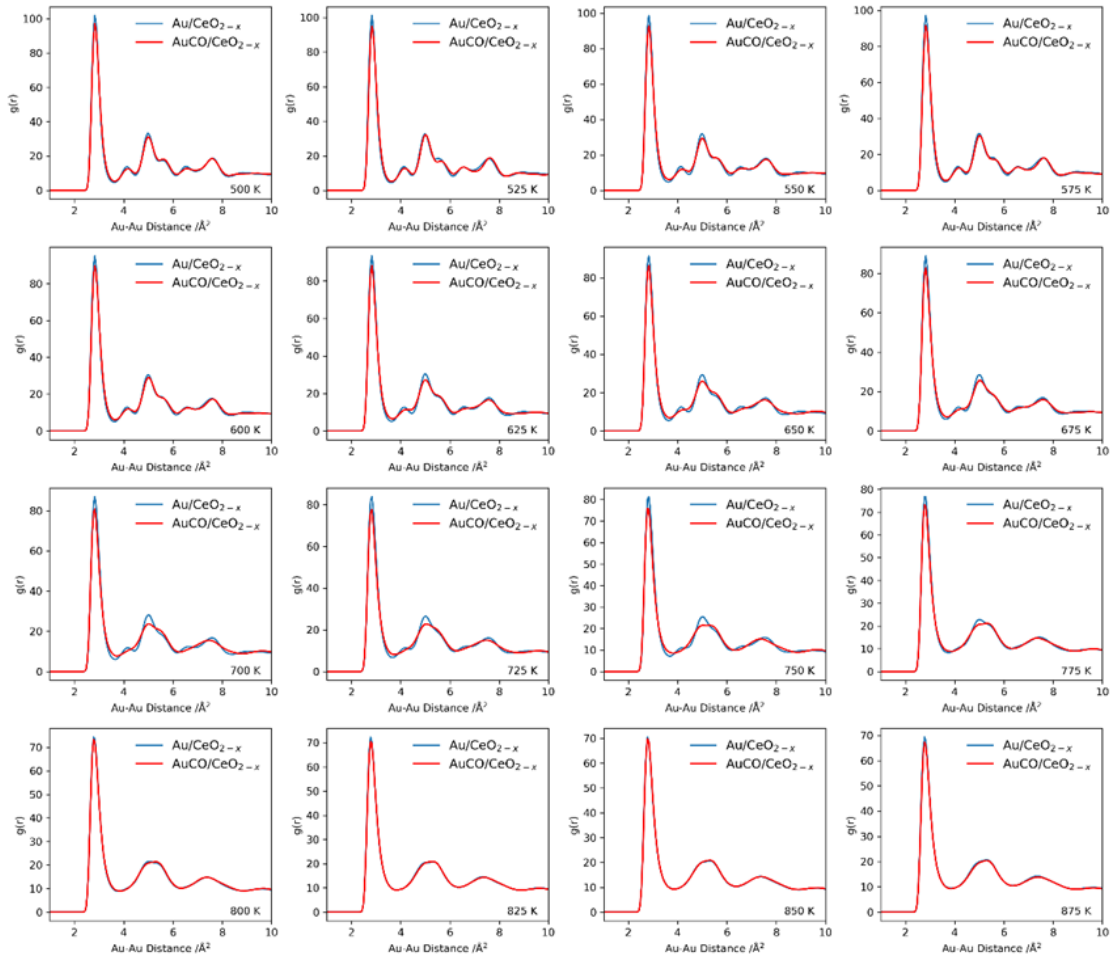

Fig. S13.

RDF of Au-Au pair for Au_{287}/CeO_{2-x} and $Au_{287}CO/CeO_{2-x}$ from 500 K to 875 K.

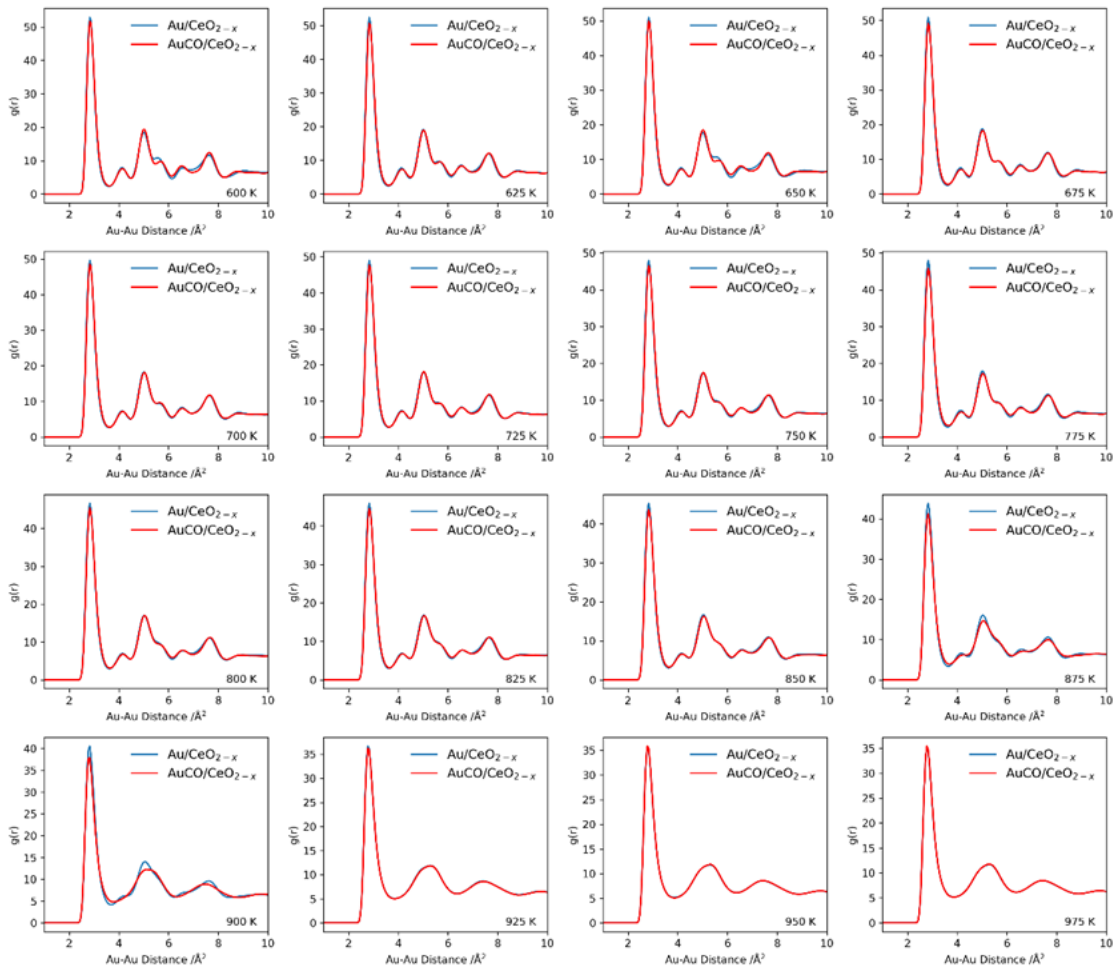

Fig. S14.

RDF of Au-Au pair for Au_{576}/CeO_{2-x} and $Au_{576}CO/CeO_{2-x}$ from 600 K to 975 K.

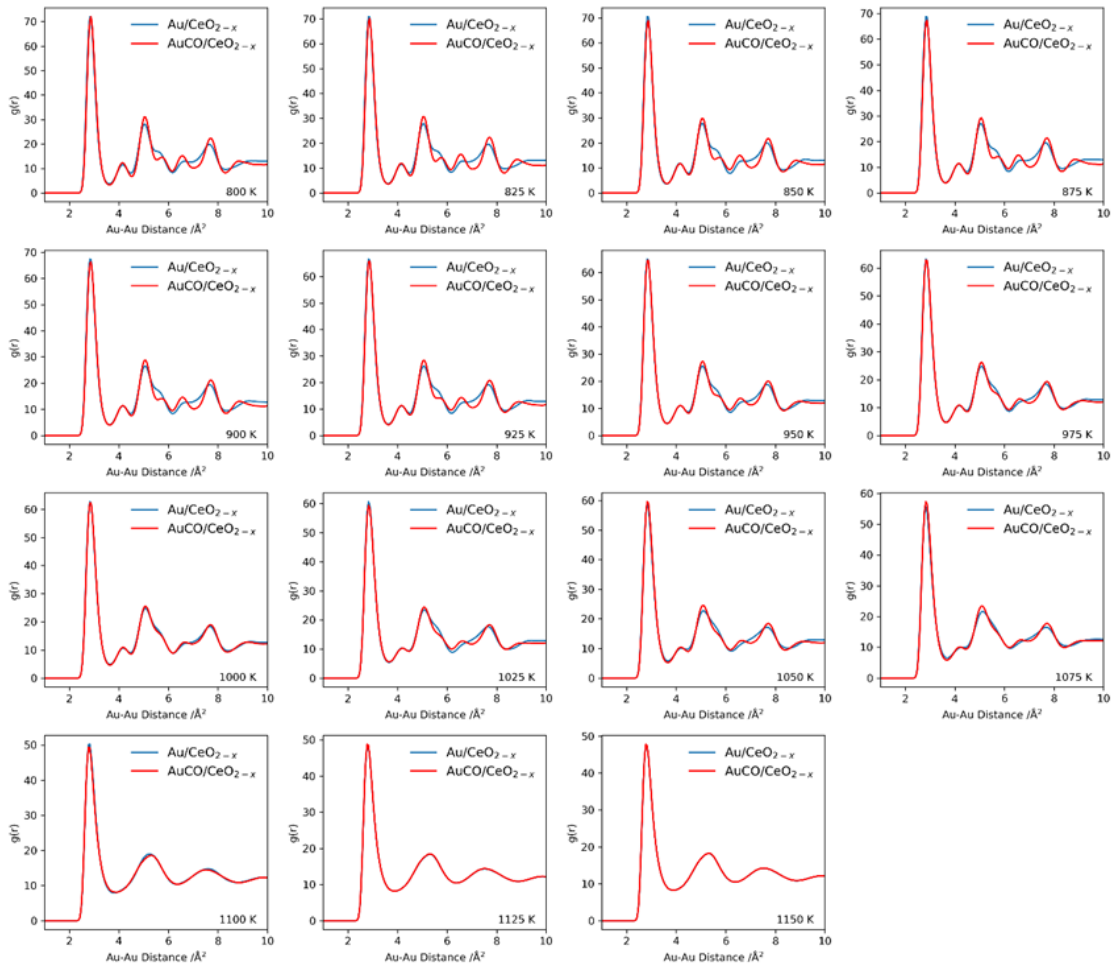

Fig. S15.

RDF of Au-Au pair for Au_{2791}/CeO_{2-x} and $Au_{2791}CO/CeO_{2-x}$ from 800 K to 1150 K.

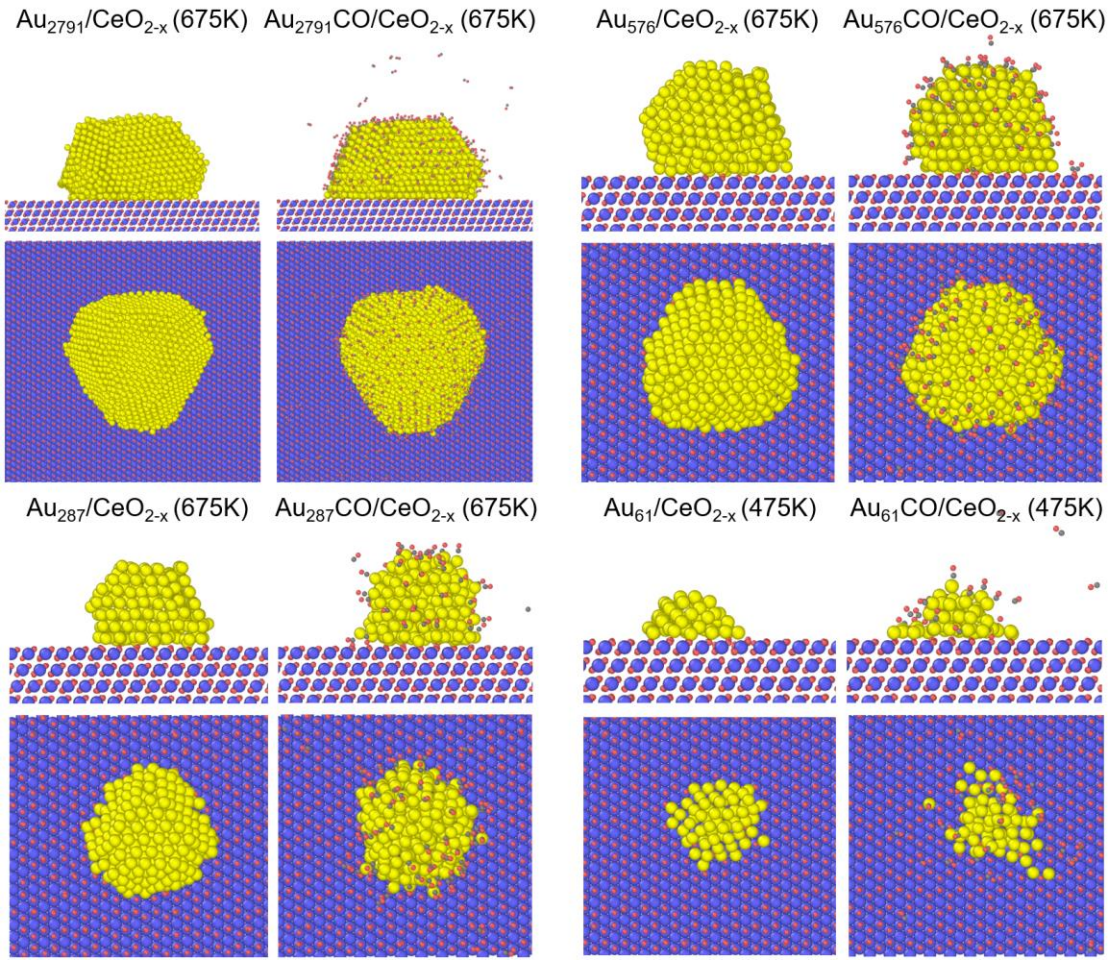

Fig. S16.

Top and side views of DPMD snapshots of $Au_{61}/CeO_{2-x}(111)$, $Au_{287}/CeO_{2-x}(111)$, $Au_{576}/CeO_{2-x}(111)$, and $Au_{2791}/CeO_{2-x}(111)$ with and without CO atmosphere at 200 ps.

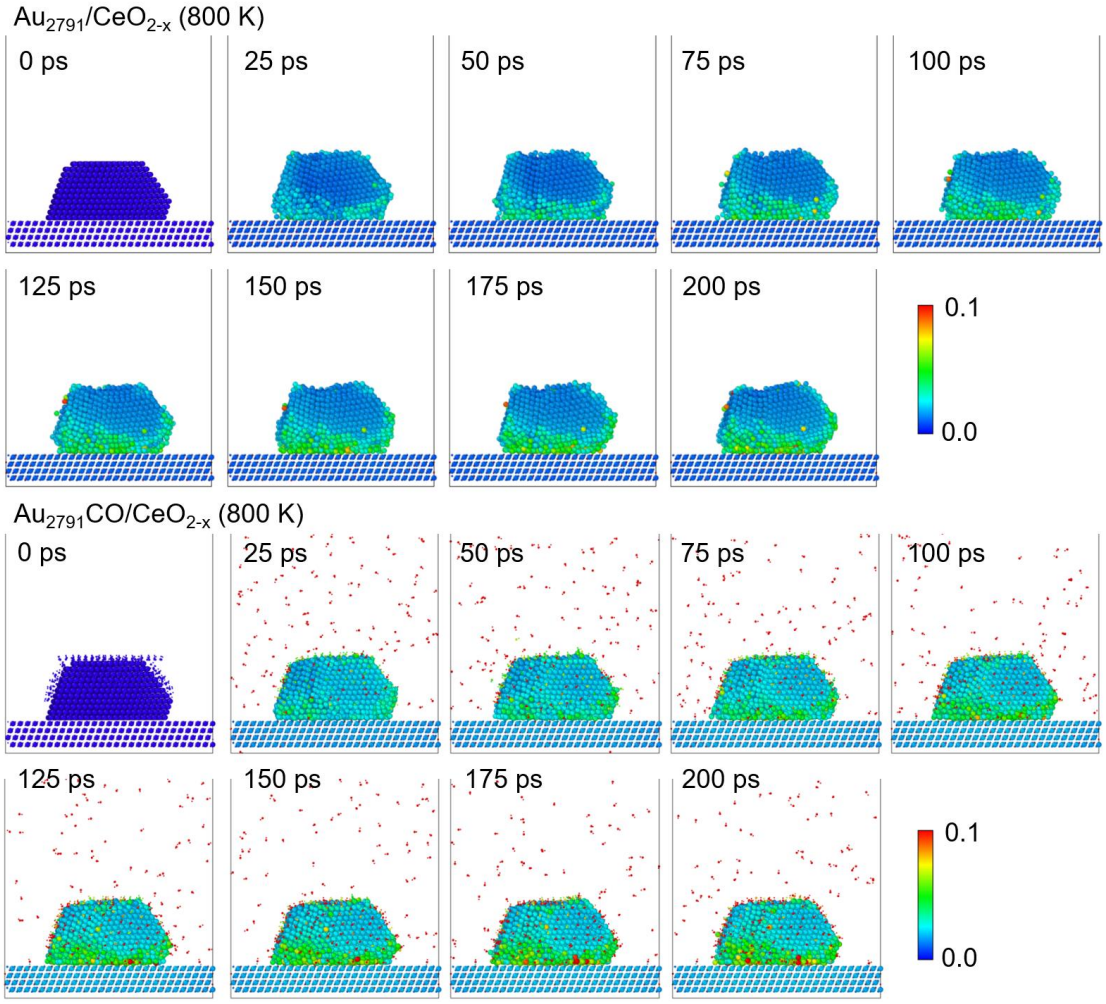

Fig. S17.

Local Lindemann index snapshots at different time steps during the DPMD simulations for Au_{2791}/CeO_{2-x} and $Au_{2791}CO/CeO_{2-x}$ at 800 K.

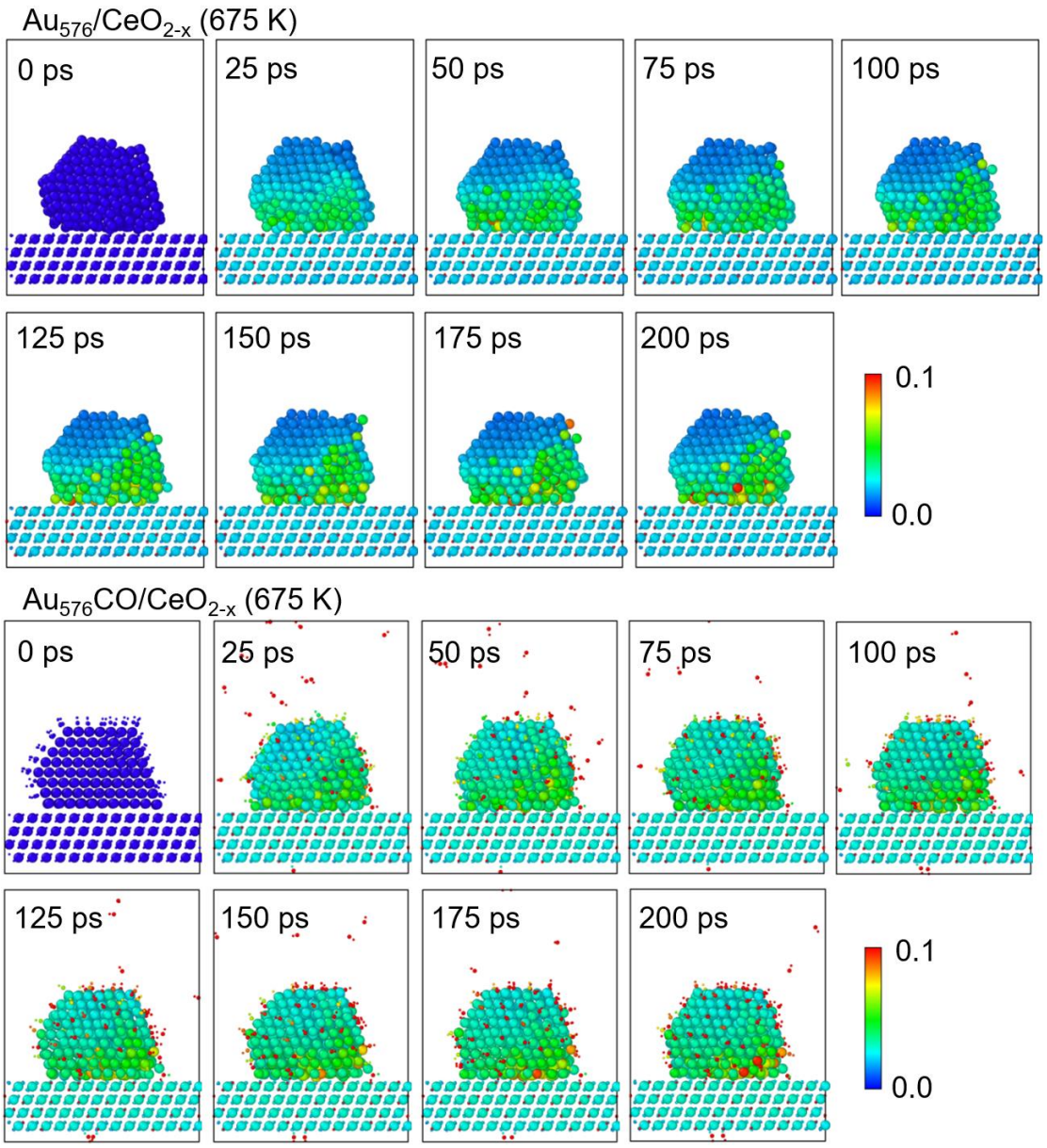

Fig. S18.

Local Lindemann index snapshots at different time steps during the DPMD simulations for Au_{576}/CeO_{2-x} and $Au_{576}CO/CeO_{2-x}$ at 675 K.

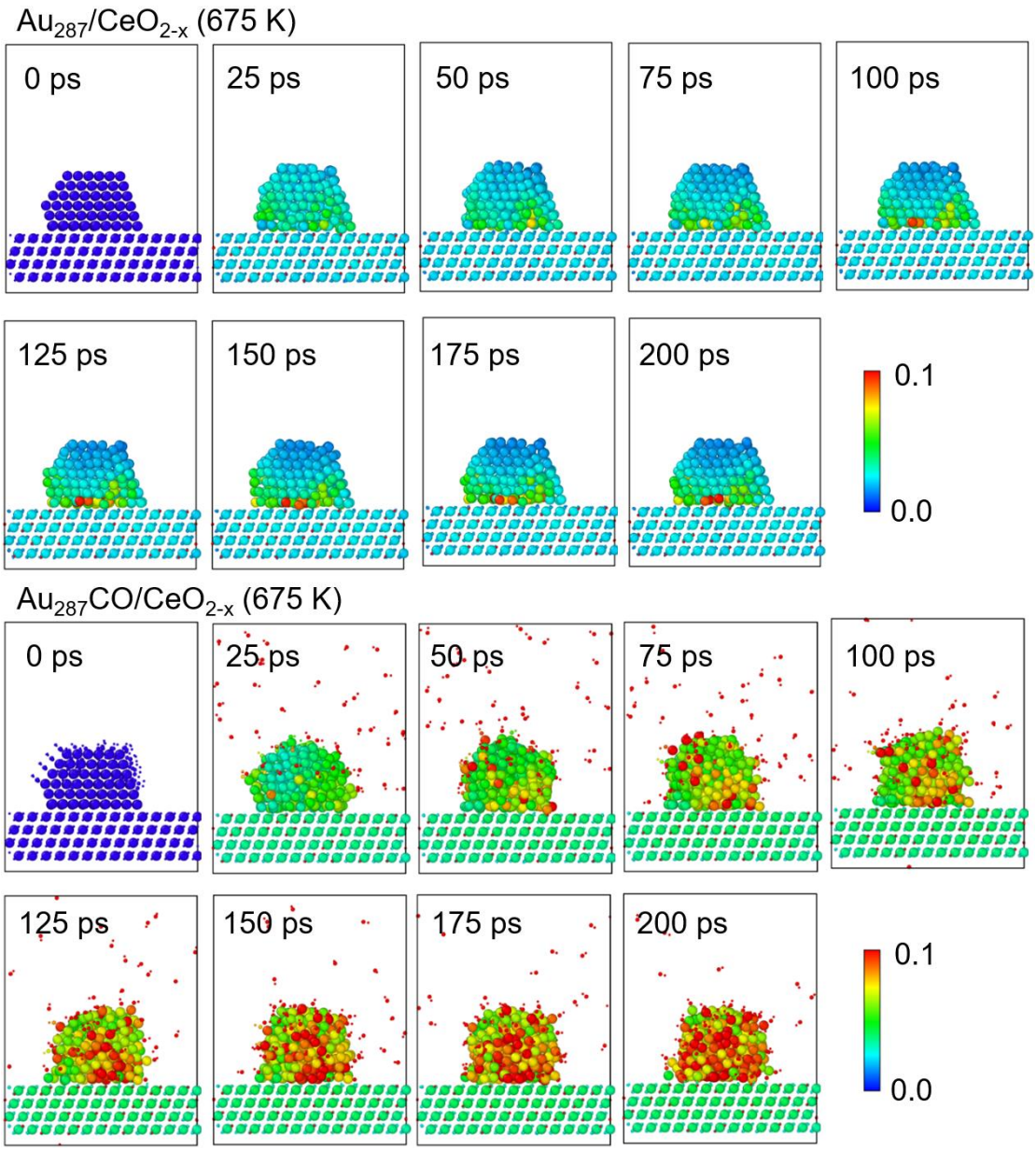

Fig. S19.

Local Lindemann index snapshots at different time steps during the DPMD simulations for Au_{287}/CeO_{2-x} and $Au_{287}CO/CeO_{2-x}$ at 675 K.

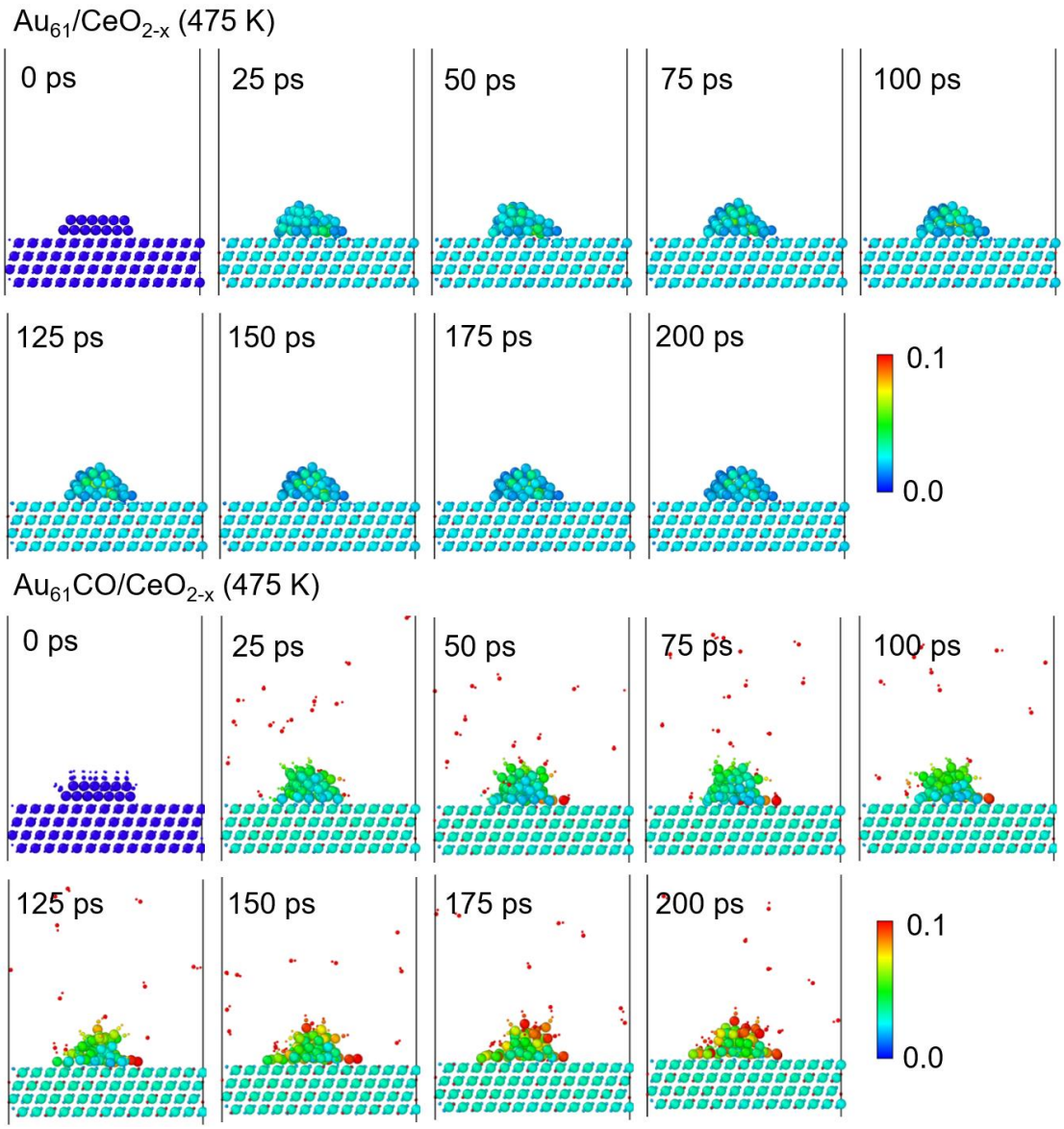

Fig. S20.

Local Lindemann index snapshots at different time steps during the DPMD simulations for Au_{61}/CeO_{2-x} and $Au_{61}CO/CeO_{2-x}$ at 475 K.

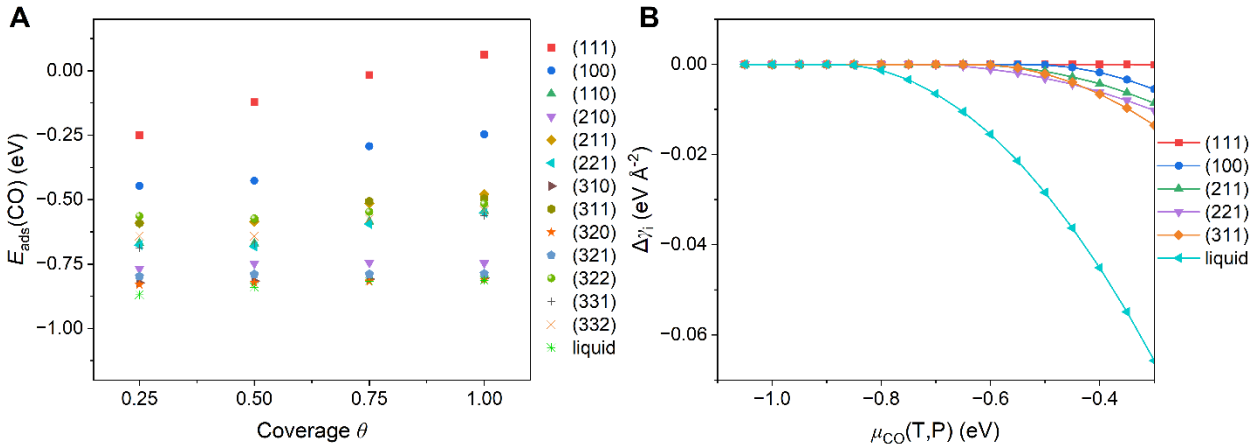

Fig. S21.

The adsorption energies of CO and corresponding change of surface energies. (A) Calculated CO adsorption energies on Au(111), Au(110), Au(100), Au(210), Au(211), Au(221), Au(310), Au(311), Au(320), Au(321), Au(322), Au(331), Au(332), and liquid Au surface versus coverage θ (ML). (B) The change of reduced surface energy, $\Delta\gamma_i(T, P)$, versus the chemical potential of CO, $\mu_{CO}(T, P)$.

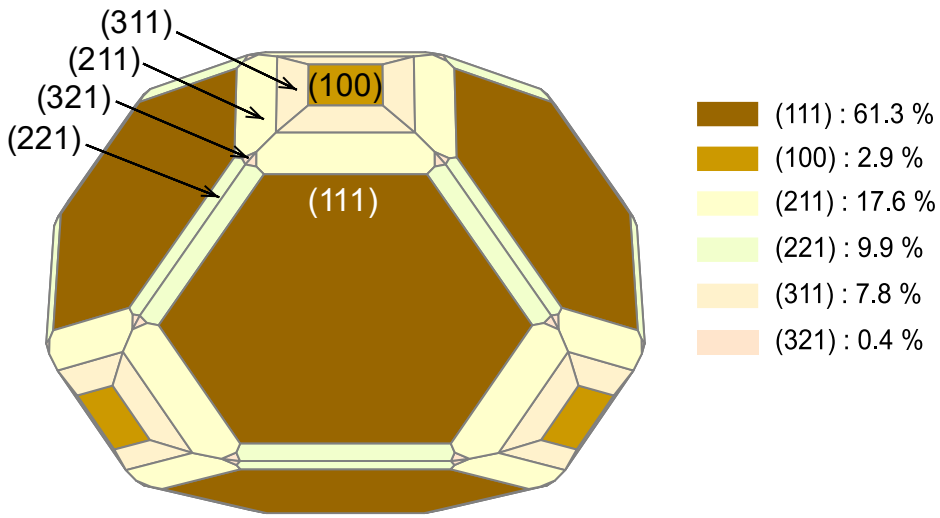

Fig. S22.

The Wulff shape of Au NPs generated with surface energies for facets up to a max Miller index of 3 in a vacuum with corresponding surface areas.

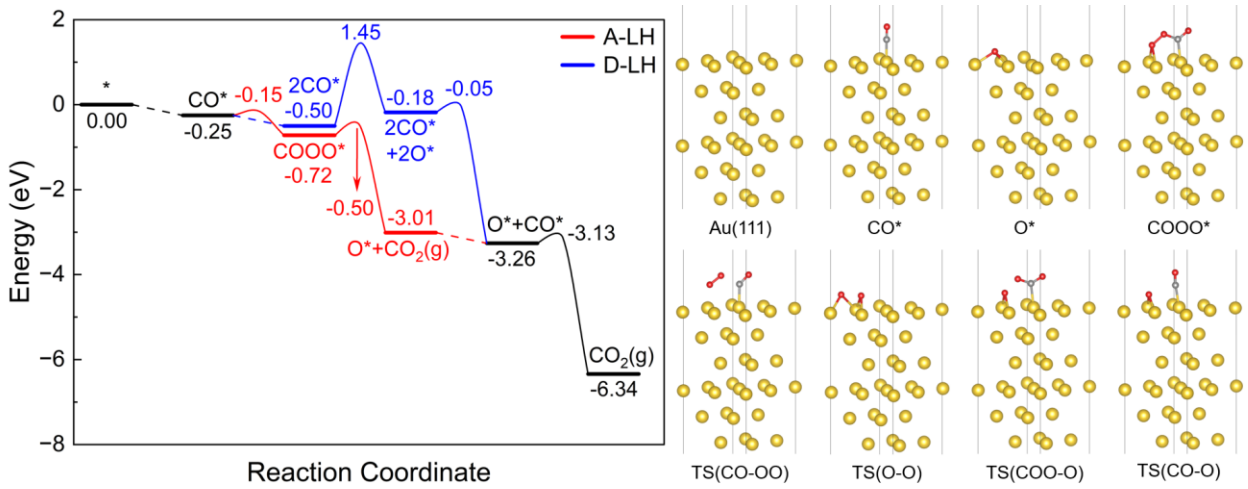

Fig. S23.

Energy profile and structures of intermediates and transition states of CO oxidation on Au(111) surface by L-H mechanism.

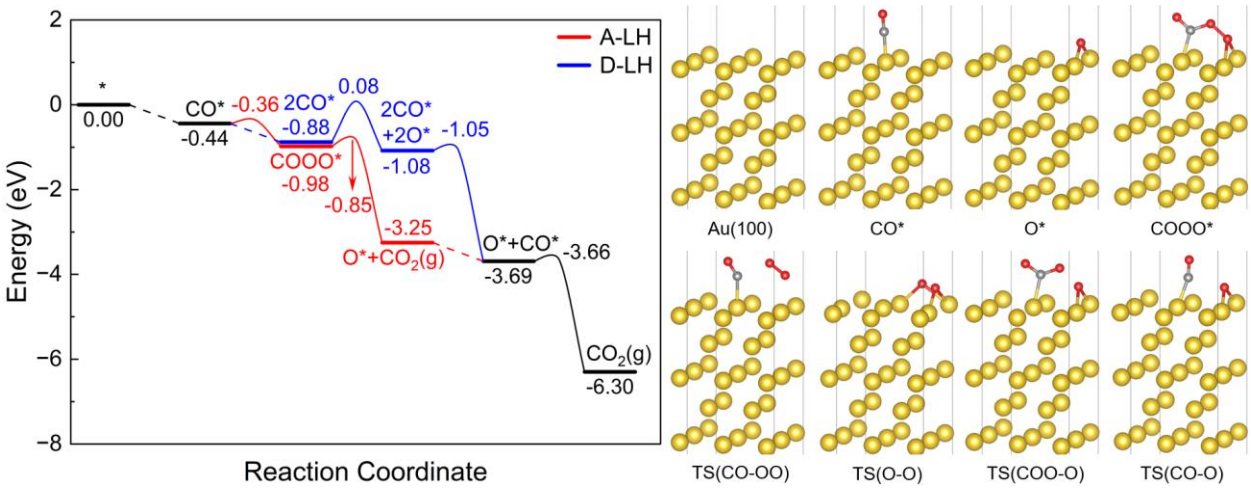

Fig. S24.

Energy profile and structures of intermediates and transition states of CO oxidation on Au(100) surface by L-H mechanism.

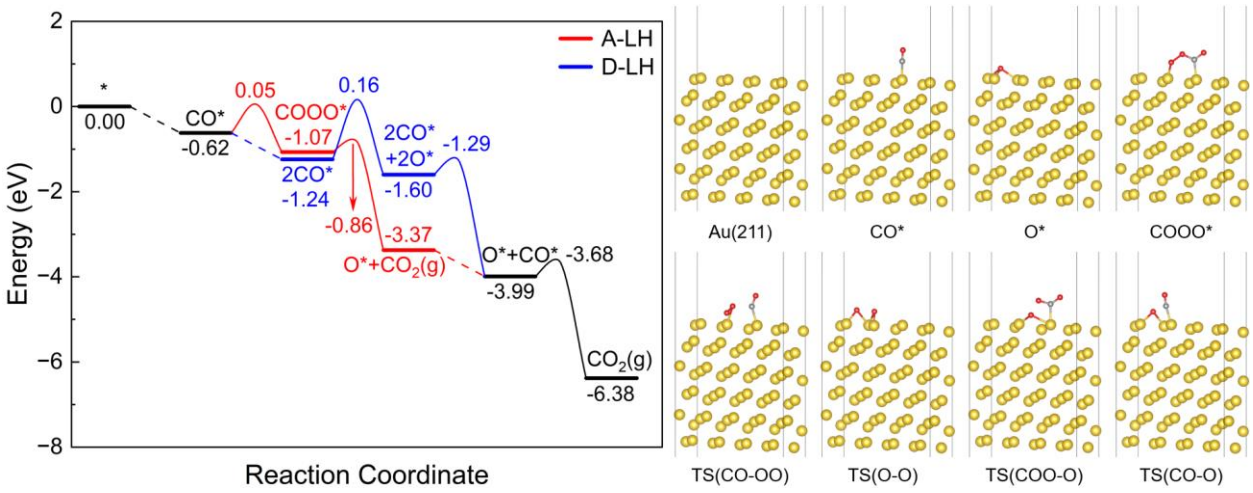

Fig. S25.

Energy profile and structures of intermediates and transition states of CO oxidation on Au(211) surface by L-H mechanism.

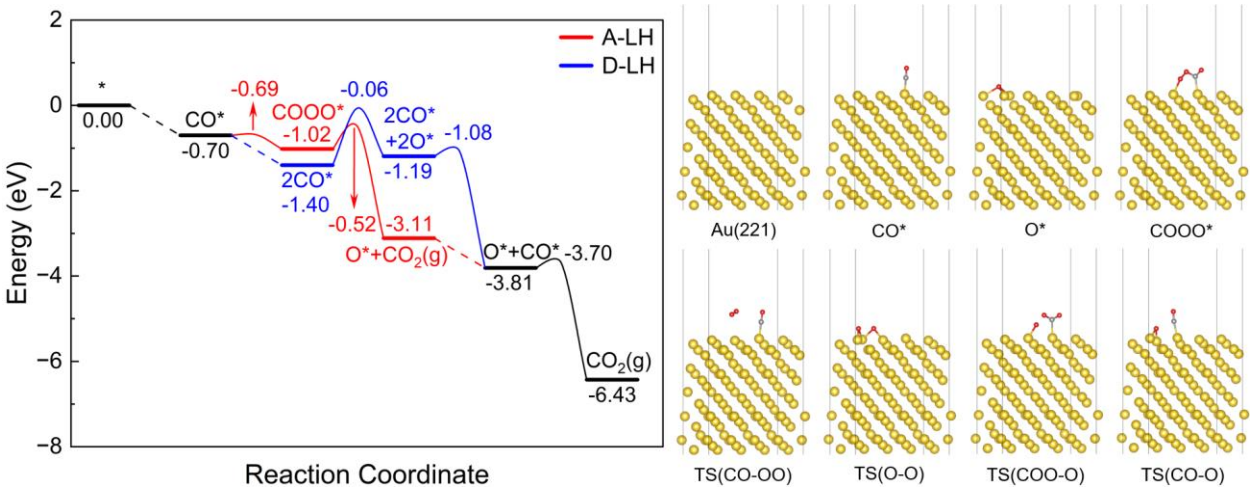

Fig. S26.

Energy profile and structures of intermediates and transition states of CO oxidation on Au(221) surface by L-H mechanism.

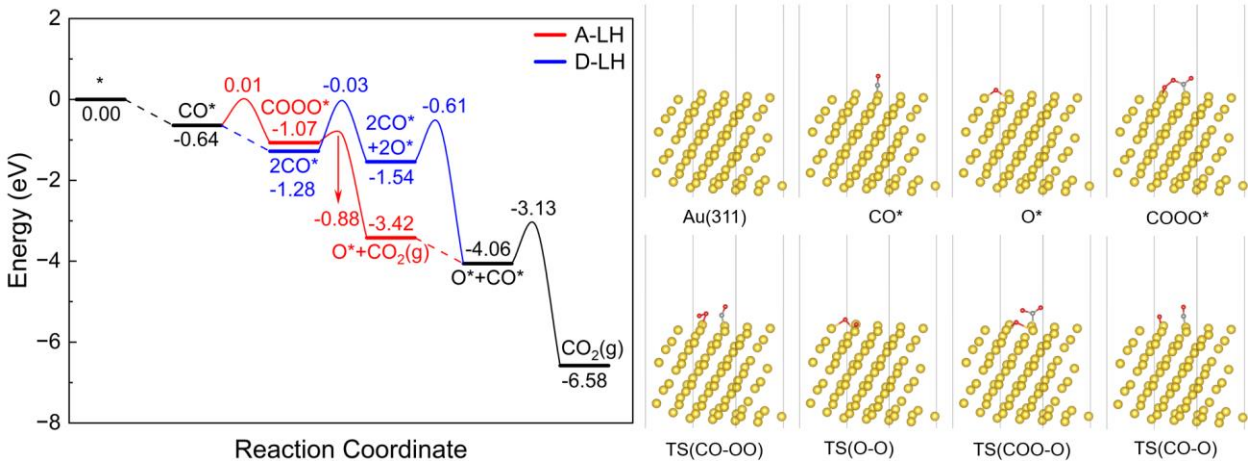

Fig. S27.

Energy profile and structures of intermediates and transition states of CO oxidation on Au(311) surface by L-H mechanism.

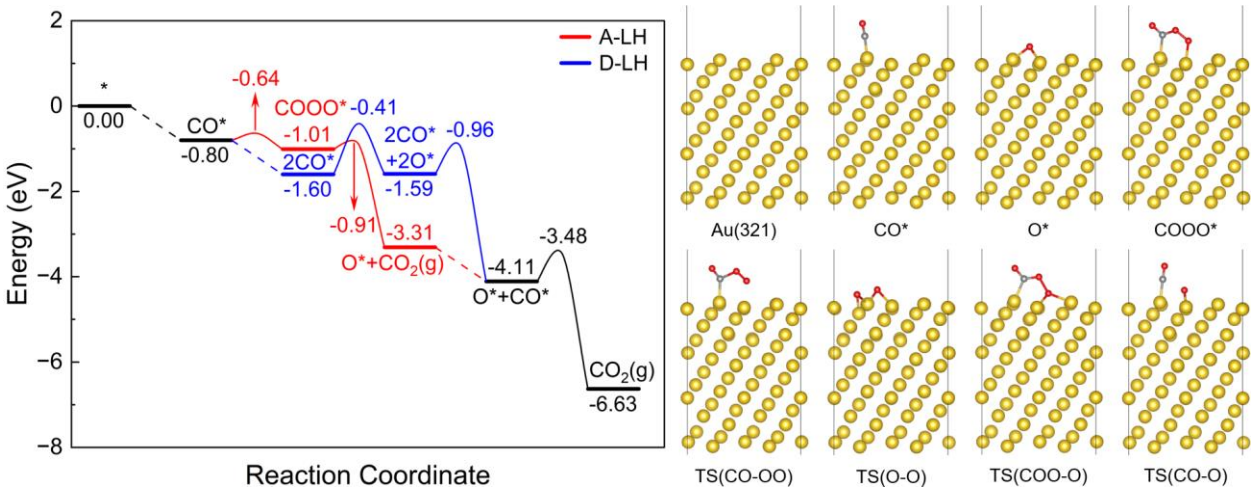

Fig. S28.

Energy profile and structures of intermediates and transition states of CO oxidation on Au(321) surface by L-H mechanism.

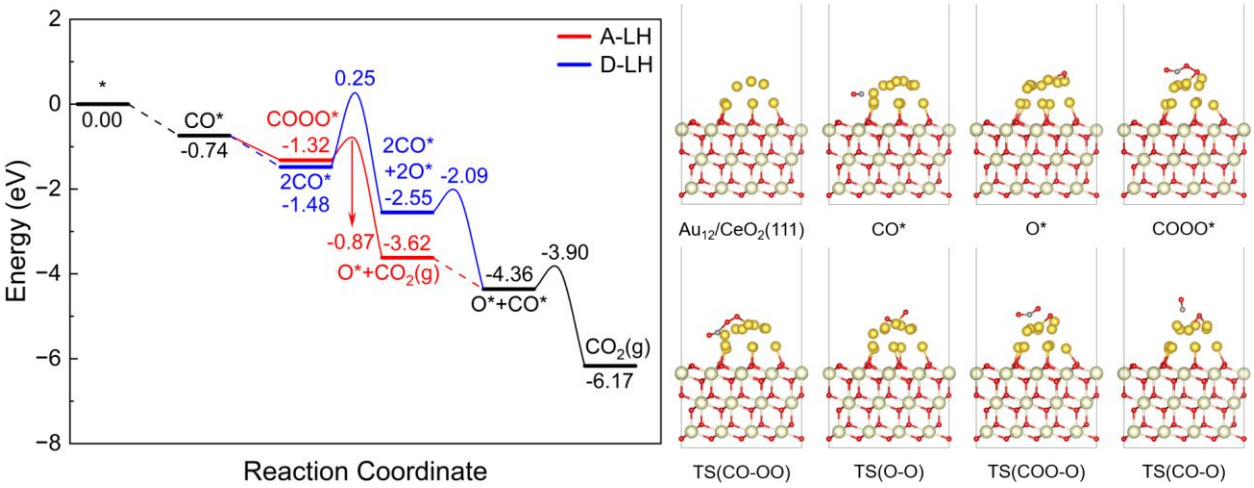

Fig. S29.

Energy profile and structures of intermediates and transition states of CO oxidation on $Au_{12}/CeO_2(111)$ by L-H mechanism.

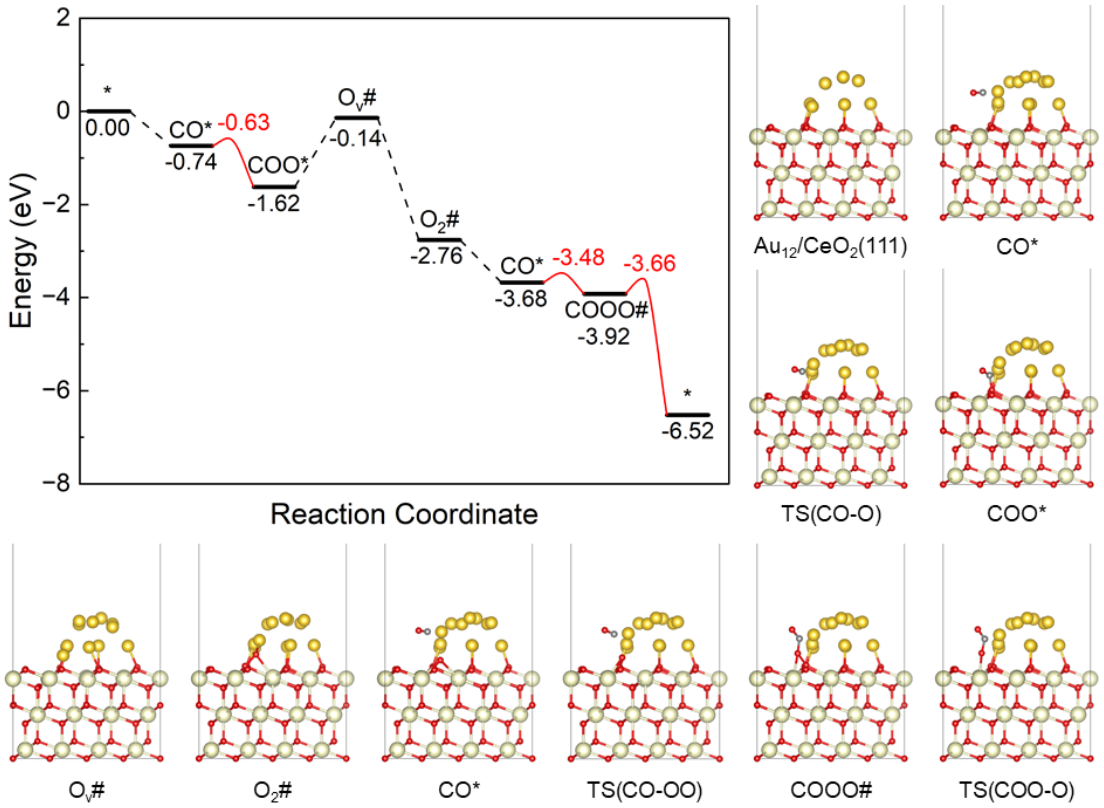

Fig. S30.

Energy profile and structures of intermediates and transition states of CO oxidation on $Au_{12}/CeO_2(111)$ interfaces by M-vK mechanism.

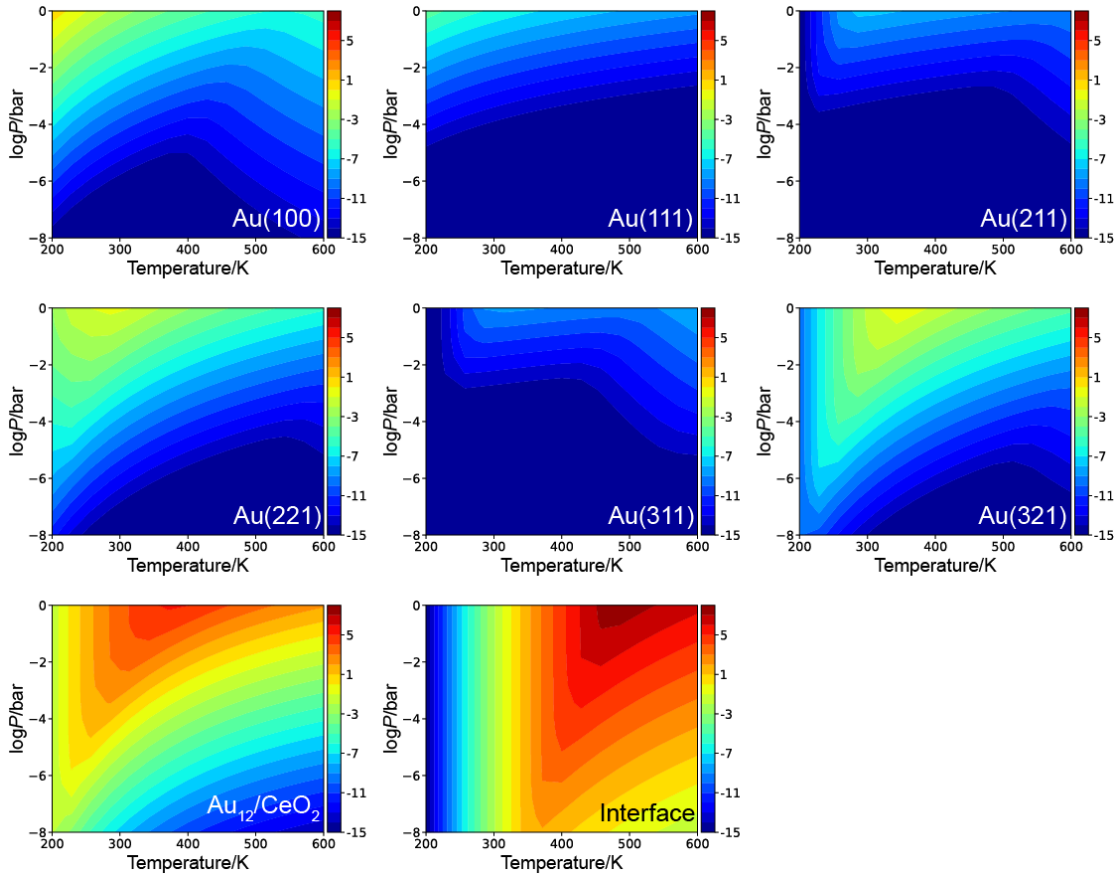

Fig. S31.

TOF of Au(100), Au(111), Au(211), Au(221), Au(311), Au(321), Au site on Au_{12}/CeO_2, and Au_{12}/CeO_2 interface at a range of total pressure from 10^{-8} to 1 bar and range of temperature from 200 to 600 K. The ratio of CO is set to 0.01 and the ratio of O_2 is set to 0.2.

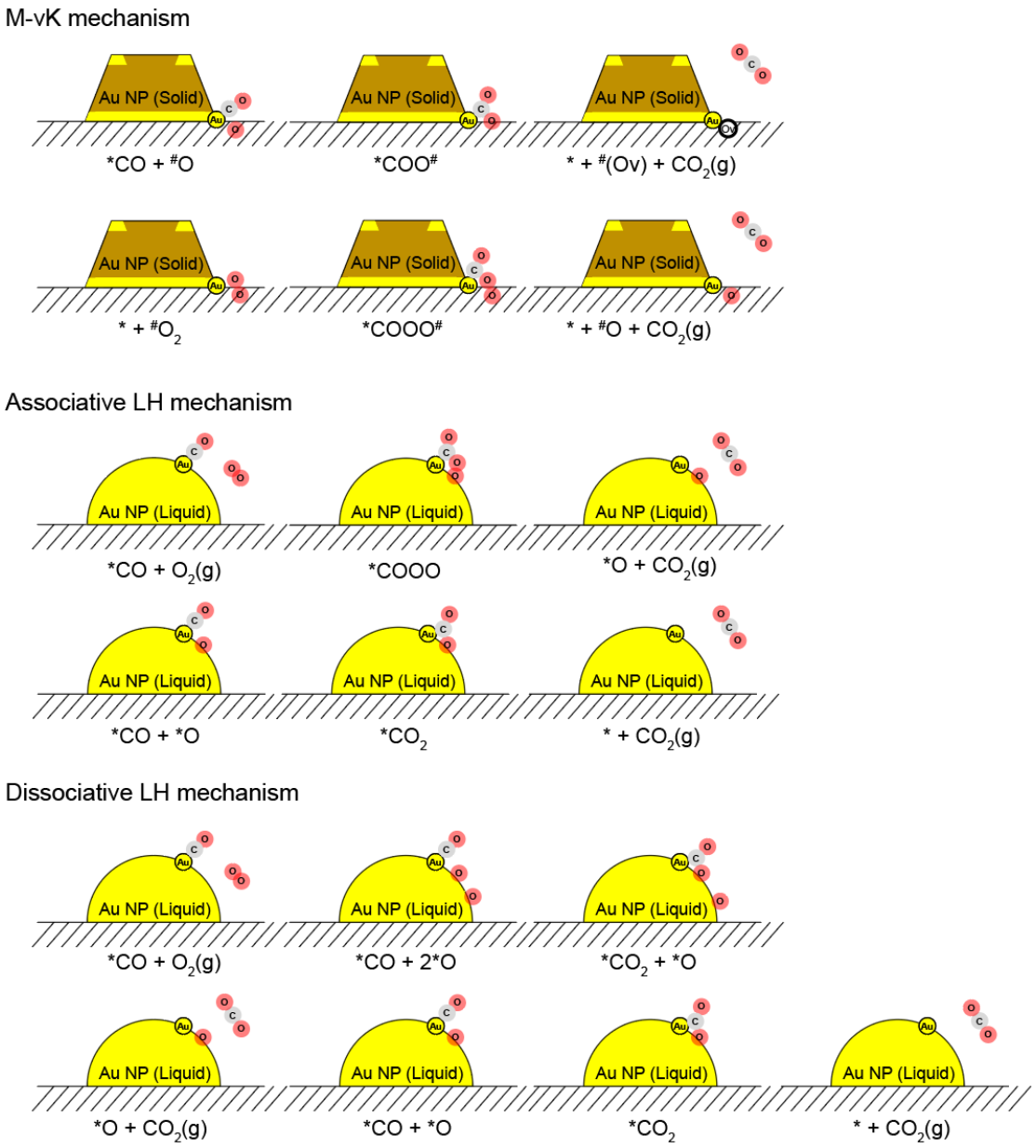

Fig. S32.

Schematic illustration of Mars-van Krevelen (M-vK), associative and dissociative Langmuir-Hinshelwood (L-H) mechanisms of CO oxidation reaction on Au/CeO_2.

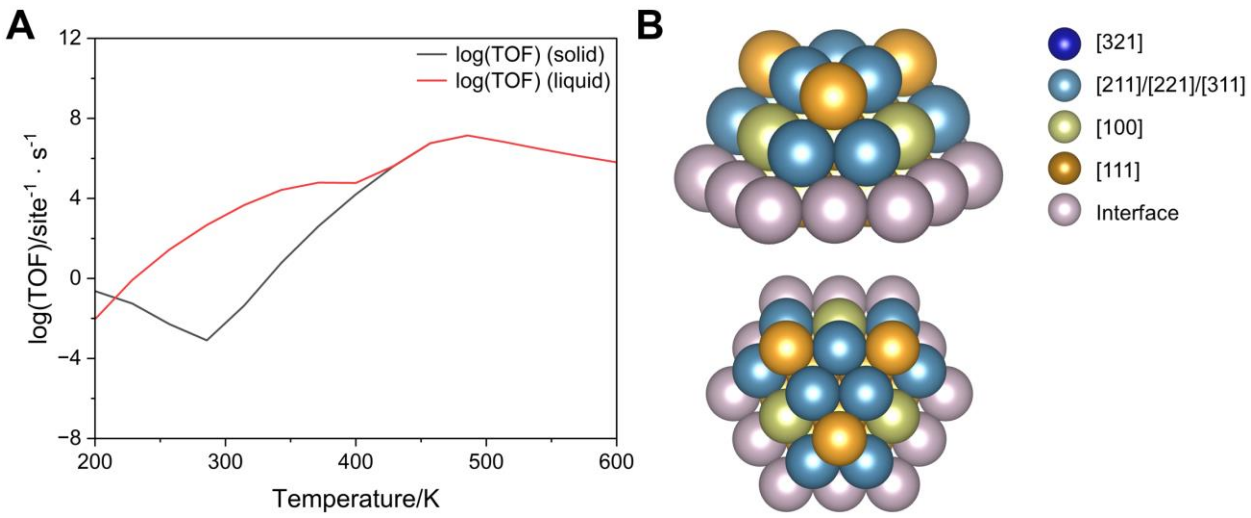

Fig. S33.

The TOF of CO_2 and corresponding structure of Au_{37} NP. (A) TOF of CO_2 versus given temperature on Au_{37} NP at P_{CO} = 0.01 bar and P_{O2} = 0.2 bar for the states of solid and liquid. (B) Structure of the Au_{37} NP from different perspectives, where the atoms with specific colors represent the corresponding surfaces or interface.

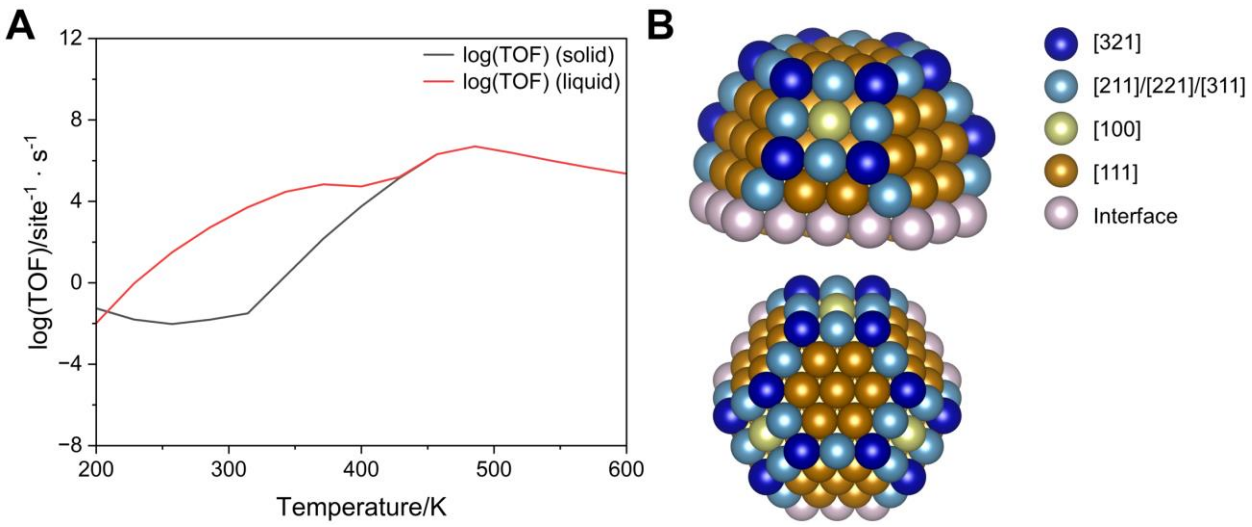

Fig. S34.

The TOF of CO_2 and corresponding structure of Au_{155} NP. (A) TOF of CO_2 versus given temperature on Au_{155} NP at P_{CO} = 0.01 bar and P_{O2} = 0.2 bar for the states of solid and liquid. (B) Structure of the Au_{155} NP from different perspectives, where the atoms with specific colors represent the corresponding surfaces or interface.

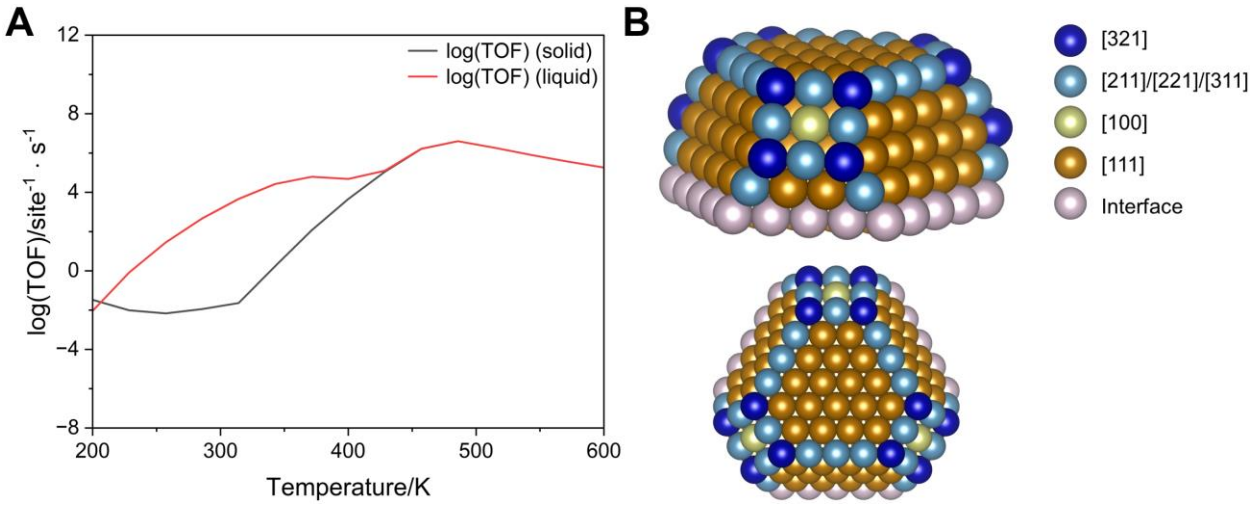

Fig. S35.

The TOF of CO_2 and corresponding structure of Au_{260} NP. (A) TOF of CO_2 versus given temperature on Au_{260} NP at P_{CO} = 0.01 bar and P_{O2} = 0.2 bar for the states of solid and liquid. (B) Structure of the Au_{260} NP from different perspectives, where the atoms with specific colors represent the corresponding surfaces or interface.

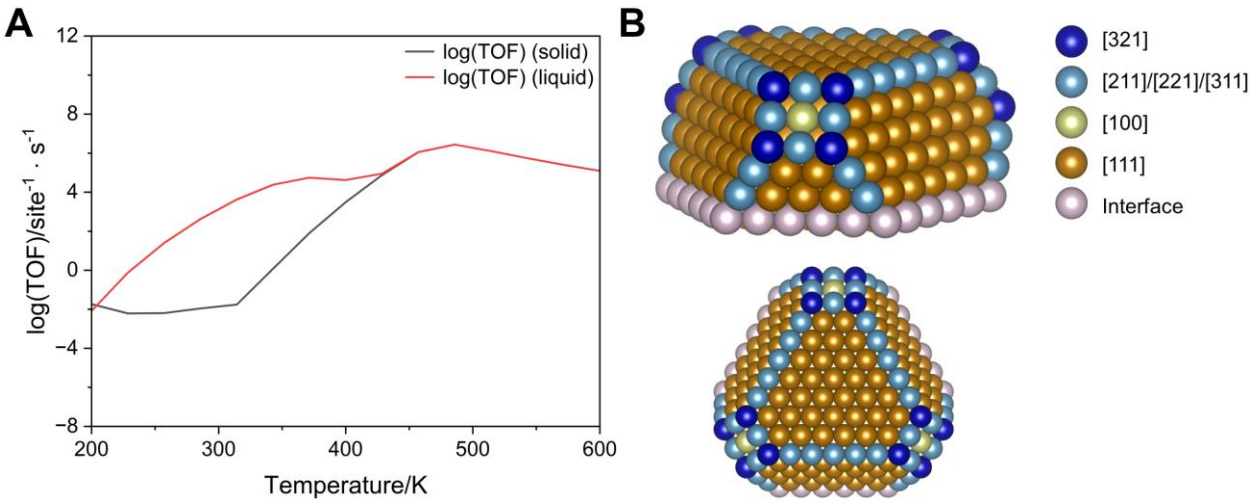

Fig. S36.

The TOF of CO_2 and corresponding structure of Au_{476} NP. (A) TOF of CO_2 versus given temperature on Au_{476} NP at P_{CO} = 0.01 bar and P_{O2} = 0.2 bar for the states of solid and liquid. (B) Structure of the Au_{476} NP from different perspectives, where the atoms with specific colors represent the corresponding surfaces or interface.

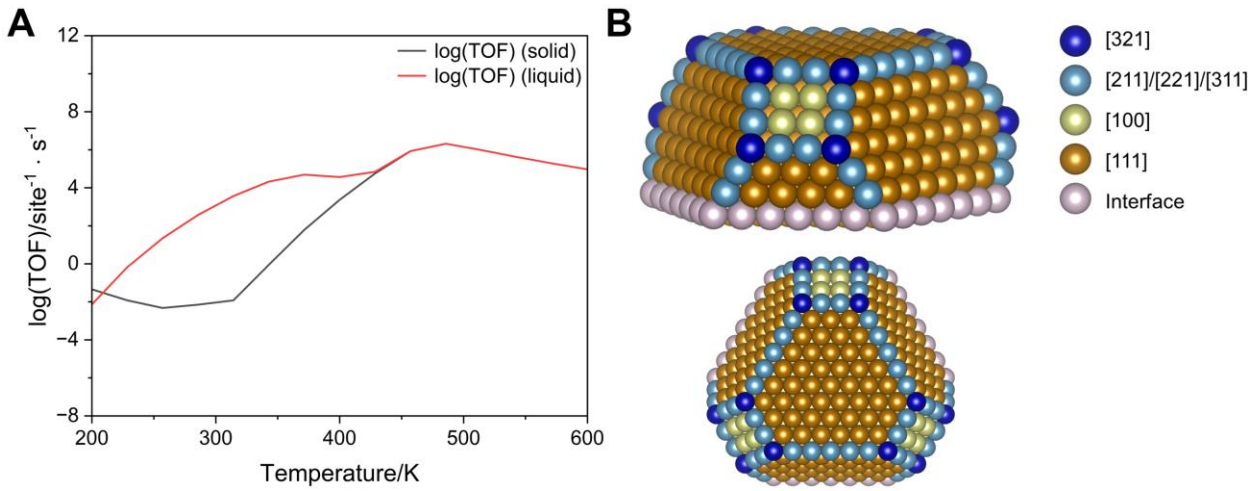

Fig. S37.

The TOF of CO_2 and corresponding structure of Au_{756} NP. (A) TOF of CO_2 versus given temperature on Au_{756} NP at P_{CO} = 0.01 bar and P_{O2} = 0.2 bar for the states of solid and liquid. (B) Structure of the Au_{756} NP from different perspectives, where the atoms with specific colors represent the corresponding surfaces or interface.

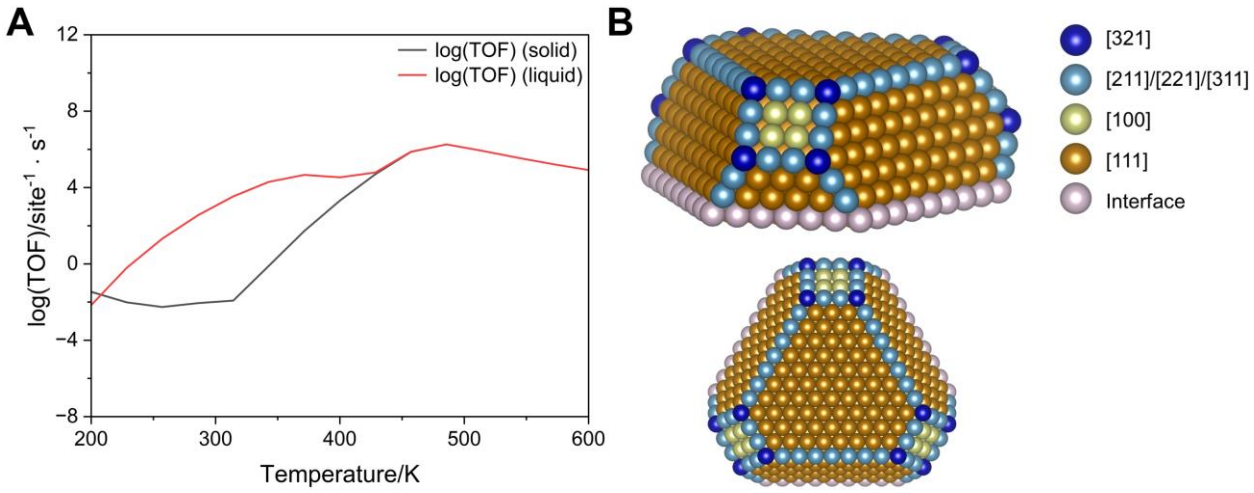

Fig. S38.

The TOF of CO_2 and corresponding structure of Au_{1001} NP. (A) TOF of CO_2 versus given temperature on Au_{1001} NP at P_{CO} = 0.01 bar and P_{O2} = 0.2 bar for the states of solid and liquid. (B) Structure of the Au_{1001} NP from different perspectives, where the atoms with specific colors represent the corresponding surfaces or interface.

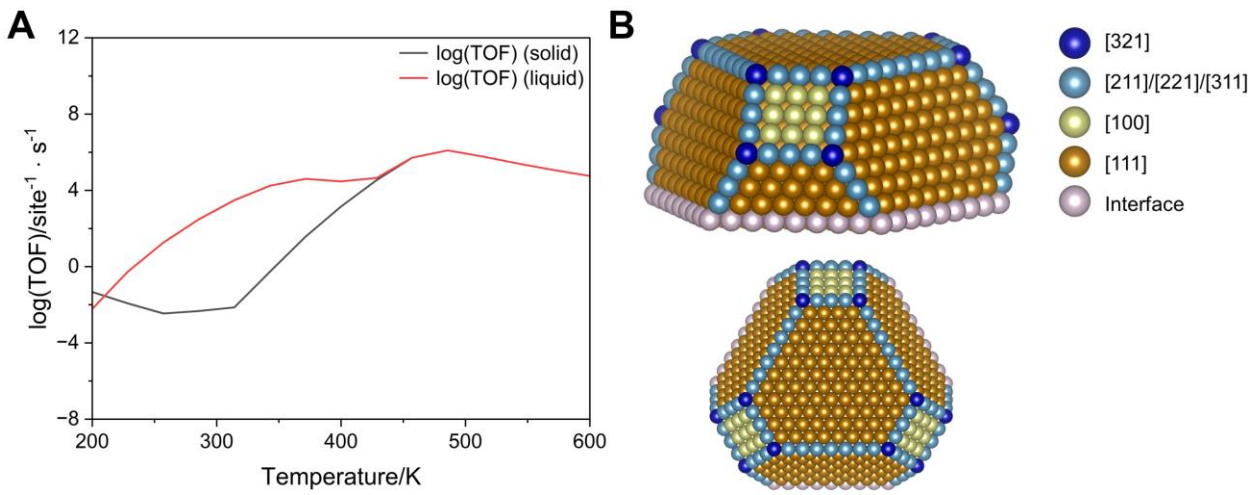

Fig. S39.

The TOF of CO_2 and corresponding structure of Au_{1659} NP. (A) TOF of CO_2 versus given temperature on Au_{1659} NP at P_{CO} = 0.01 bar and P_{O2} = 0.2 bar for the states of solid and liquid. (B) Structure of the Au_{1659} NP from different perspectives, where the atoms with specific colors represent the corresponding surfaces or interface.

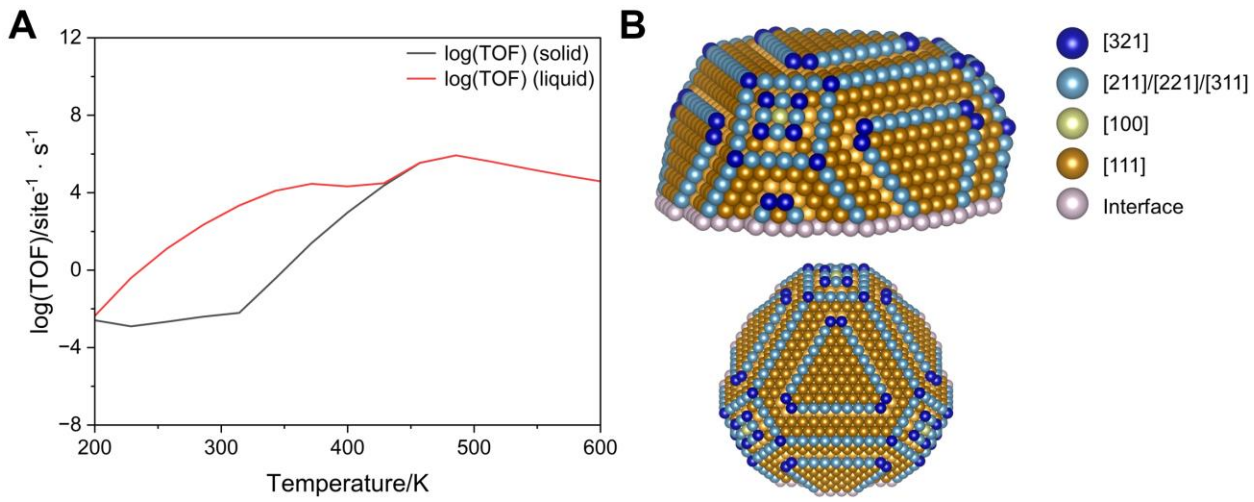

Fig. S40.

The TOF of CO_2 and corresponding structure of Au_{3382} NP. (A) TOF of CO_2 versus given temperature on Au_{3382} NP at P_{CO} = 0.01 bar and P_{O2} = 0.2 bar for the states of solid and liquid. (B) Structure of the Au_{3382} NP from different perspectives, where the atoms with specific colors represent the corresponding surfaces or interface.

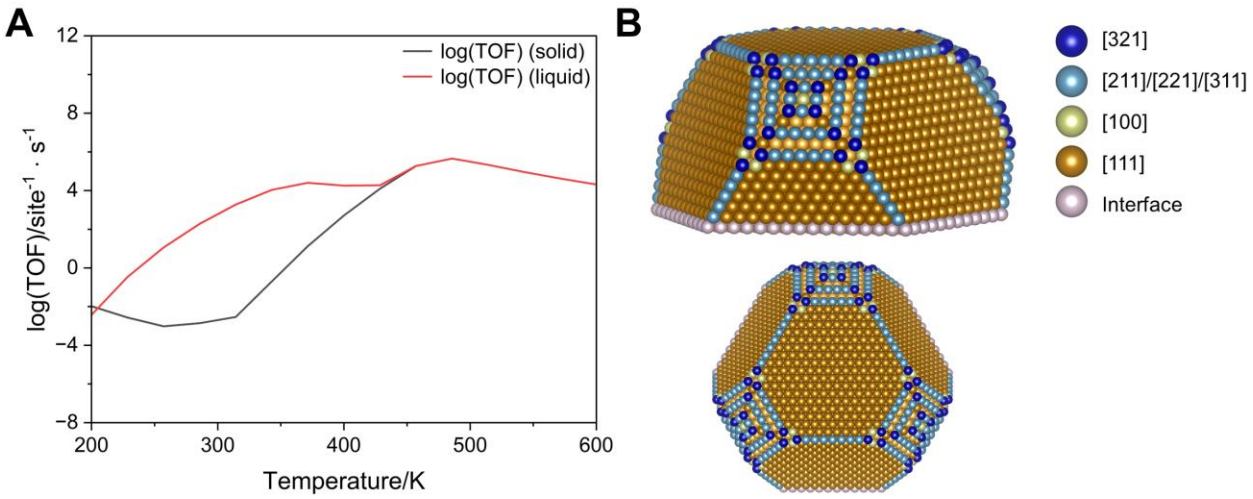

Fig. S41.

The TOF of CO_2 and corresponding structure of Au_{7439} NP. (A) TOF of CO_2 versus given temperature on Au_{7439} NP at P_{CO} = 0.01 bar and P_{O2} = 0.2 bar for the states of solid and liquid. (B) Structure of the Au_{7439} NP from different perspectives, where the atoms with specific colors represent the corresponding surfaces or interface.

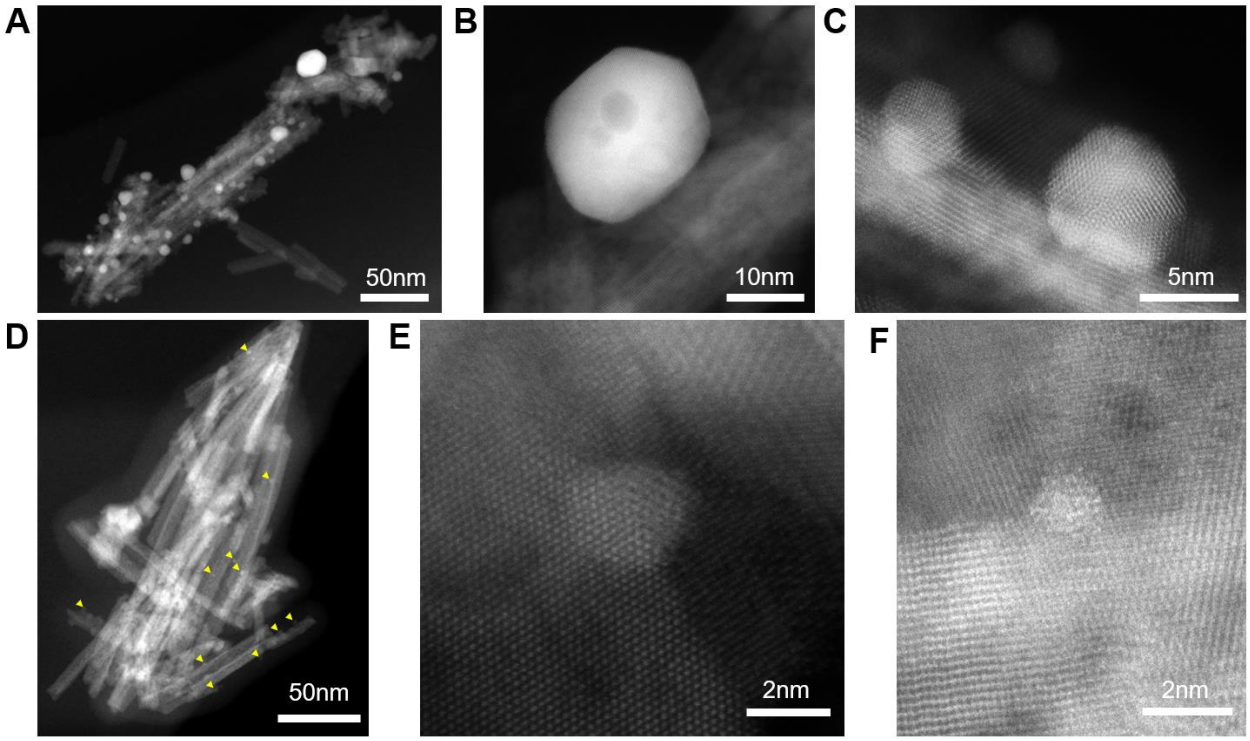

Fig. S42.

Large area and enlarged HAADF images showing the large (A-C) and small (D-F) Au supported on CeO_2.

Table S1.

Ratios of surface tensions of solid and liquid Au in comparison to other calculations and experiments.

	(*hkl*)	This work	*Calc.(16)*	*Calc.(17)*	*Exp.(20)*
Solid Surface	$\gamma_{(111)}$	0.709 J/m^2	0.69 J/m^2	0.64 J/m^2	1.38 J/m^2
	$\gamma_{(100)}/\gamma_{(111)}$	1.289	1.23	1.11	
	$\gamma_{(110)}/\gamma_{(111)}$	1.310	1.29	1.24	
	$\gamma_{(210)}/\gamma_{(111)}$	1.290	1.33	1.31	
	$\gamma_{(211)}/\gamma_{(111)}$	1.162	1.17	1.19	
	$\gamma_{(221)}/\gamma_{(111)}$	1.127	1.14	1.16	
	$\gamma_{(310)}/\gamma_{(111)}$	1.297	1.31	1.28	
	$\gamma_{(311)}/\gamma_{(111)}$	1.229	1.26	1.24	
	$\gamma_{(320)}/\gamma_{(111)}$	1.314	1.36	1.30	
	$\gamma_{(321)}/\gamma_{(111)}$	1.207	1.25	1.26	
	$\gamma_{(322)}/\gamma_{(111)}$	1.140	1.11	1.13	
	$\gamma_{(331)}/\gamma_{(111)}$	1.185	1.18	1.21	
	$\gamma_{(332)}/\gamma_{(111)}$	1.095	1.07	1.11	
Liquid surface					1.135 J/m^2

Table S2.

Unit surface area (A_i) and averaged CO adsorption energies in eV on solid Au(*hkl*) (*h*, *k*, and $l < 3$) surface and liquid Au surface with coverages of 1/4, 1/2, 3/4, and 1.

(*hkl*)	$E_{CO}^{ads}(\theta=1/4)$	$E_{CO}^{ads}(\theta=1/2)$	$E_{CO}^{ads}(\theta=3/4)$	$E_{CO}^{ads}(\theta=1)$	A_i (Å^2)
(111)	-0.250	-0.122	-0.017	0.062	7.48
(100)	-0.446	-0.427	-0.293	-0.246	8.63
(110)	-0.669	-0.670	-0.585	-0.544	12.21
(210)	-0.768	-0.748	-0.745	-0.746	19.30
(211)	-0.592	-0.585	-0.515	-0.478	21.14
(221)	-0.676	-0.682	-0.595	-0.551	25.90
(310)	-0.823	-0.816	-0.808	-0.804	27.30
(311)	-0.592	-0.576	-0.506	-0.496	14.31
(320)	-0.830	-0.823	-0.817	-0.811	31.12
(321)	-0.798	-0.790	-0.789	-0.788	32.30
(322)	-0.564	-0.573	-0.547	-0.516	35.59
(331)	-0.687	-0.672	-0.598	-0.562	18.81
(332)	-0.641	-0.642	-0.575	-0.541	40.49
Liquid surface	-0.869	-0.840	-0.817	-0.813	17.01

Table S3.

The slope *a* and intercept *b* of the linear fitting.

(*hkl*)	*a*	*b*
(111)	0.417	-0.343
(100)	0.293	-0.536
(110)	0.183	-0.732
(210)	0.0276	-0.769
(211)	0.165	-0.646
(221)	0.185	-0.742
(310)	0.026	-0.829
(311)	0.142	-0.631
(320)	0.0252	-0.836
(321)	0.0124	-0.799
(322)	0.067	-0.592
(331)	0.180	-0.742
(332)	0.147	-0.692
Liquid surface	0.076	-0.883

Table S4.

Thermodynamic data for gas CO molecules concerning that at T = 0 K from JANAF-NIST standard thermodynamic tables.

T (K)	S-S_0 J mol^{-1} K^{-1}	H-H_0 kJ mol^{-1}	$\mu_{CO}(T, P^{\emptyset})$ kJ mol^{-1}	$\mu_{CO}(T, P^{\emptyset})$ eV	$\mu_{CO}(T, P = 10^{-2} bar)$ eV
0.00	0.00	-8.67	0.00	0.00	0.00
100.00	165.85	-5.77	-13.68	-0.14	-0.18
200.00	186.03	-2.86	-31.39	-0.33	-0.40
300.00	197.83	0.05	-50.62	-0.52	-0.64
400.00	206.24	2.98	-70.85	-0.73	-0.89
500.00	212.83	5.93	-91.81	-0.95	-1.15
600.00	218.32	8.94	-113.38	-1.18	-1.41
700.00	223.07	12.02	-135.45	-1.40	-1.68
800.00	227.28	15.18	-157.97	-1.64	-1.95
900.00	231.07	18.40	-180.89	-1.87	-2.23
1000.00	234.54	21.69	-204.18	-2.12	-2.51

Table S5.

$\Delta\gamma_i$ at different chemical potential of CO, $\mu_{CO}(T, P)$.

$\mu_{CO}(T, P)$	(111)	(100)	(110)	(210)	(211)	(221)	(310)	(311)
0.00	-0.0094	-0.0284	-0.0600	-0.0390	-0.0299	-0.0287	-0.0298	-0.0490
-0.05	-0.0069	-0.0234	-0.0520	-0.0390	-0.0255	-0.0250	-0.0298	-0.0415
-0.10	-0.0047	-0.0188	-0.0447	-0.0390	-0.0214	-0.0215	-0.0298	-0.0347
-0.15	-0.0030	-0.0147	-0.0379	-0.0390	-0.0176	-0.0183	-0.0298	-0.0285
-0.20	-0.0016	-0.0112	-0.0317	-0.0390	-0.0143	-0.0153	-0.0298	-0.0229
-0.25	-0.0007	-0.0081	-0.0260	-0.0390	-0.0112	-0.0126	-0.0298	-0.0179
-0.30	-0.0001	-0.0055	-0.0209	-0.0390	-0.0086	-0.0102	-0.0298	-0.0135
-0.35	0.0000	-0.0034	-0.0163	-0.0390	-0.0063	-0.0080	-0.0298	-0.0097
-0.40	0.0000	-0.0018	-0.0123	-0.0390	-0.0043	-0.0061	-0.0298	-0.0066
-0.45	0.0000	-0.0007	-0.0089	-0.0390	-0.0028	-0.0044	-0.0298	-0.0040
-0.50	0.0000	-0.0001	-0.0060	-0.0390	-0.0015	-0.0031	-0.0298	-0.0021
-0.55	0.0000	0.0000	-0.0037	-0.0390	-0.0007	-0.0019	-0.0298	-0.0008
-0.60	0.0000	0.0000	-0.0019	-0.0390	-0.0002	-0.0011	-0.0298	-0.0001
-0.65	0.0000	0.0000	-0.0008	-0.0390	0.0000	-0.0004	-0.0298	0.0000
-0.70	0.0000	0.0000	-0.0001	-0.0390	0.0000	-0.0001	-0.0298	0.0000
-0.75	0.0000	0.0000	0.0000	-0.0390	0.0000	0.0000	-0.0298	0.0000
-0.80	0.0000	0.0000	0.0000	0.0000	0.0000	0.0000	-0.0298	0.0000
-0.85	0.0000	0.0000	0.0000	0.0000	0.0000	0.0000	0.0000	0.0000
-0.90	0.0000	0.0000	0.0000	0.0000	0.0000	0.0000	0.0000	0.0000
-0.95	0.0000	0.0000	0.0000	0.0000	0.0000	0.0000	0.0000	0.0000
-1.00	0.0000	0.0000	0.0000	0.0000	0.0000	0.0000	0.0000	0.0000
-1.05	0.0000	0.0000	0.0000	0.0000	0.0000	0.0000	0.0000	0.0000

Table S6.

$\Delta\gamma_i$ at different chemical potential of CO, $\mu_{CO}(T, P)$.

$\mu_{CO}(T, P)$	(320)	(321)	(322)	(331)	(332)	Liquid
0.00	-0.0263	-0.0245	-0.0367	-0.0407	-0.0201	-0.0263
-0.05	-0.0263	-0.0245	-0.0308	-0.0354	-0.0173	-0.0263
-0.10	-0.0263	-0.0245	-0.0254	-0.0304	-0.0147	-0.0263
-0.15	-0.0263	-0.0245	-0.0205	-0.0259	-0.0123	-0.0263
-0.20	-0.0263	-0.0245	-0.0161	-0.0217	-0.0102	-0.0263
-0.25	-0.0263	-0.0245	-0.0123	-0.0179	-0.0082	-0.0263
-0.30	-0.0263	-0.0245	-0.0089	-0.0144	-0.0065	-0.0263
-0.35	-0.0263	-0.0245	-0.0061	-0.0113	-0.0049	-0.0263
-0.40	-0.0263	-0.0245	-0.0039	-0.0086	-0.0036	-0.0263
-0.45	-0.0263	-0.0245	-0.0021	-0.0063	-0.0025	-0.0263
-0.50	-0.0263	-0.0245	-0.0009	-0.0043	-0.0015	-0.0263
-0.55	-0.0263	-0.0245	-0.0002	-0.0027	-0.0008	-0.0263
-0.60	-0.0263	-0.0245	0.0000	-0.0015	-0.0004	-0.0263
-0.65	-0.0263	-0.0245	0.0000	-0.0006	-0.0001	-0.0263
-0.70	-0.0263	-0.0245	0.0000	-0.0001	0.0000	-0.0263
-0.75	-0.0263	-0.0245	0.0000	0.0000	0.0000	-0.0263
-0.80	-0.0263	0.0000	0.0000	0.0000	0.0000	-0.0263
-0.85	0.0000	0.0000	0.0000	0.0000	0.0000	0.0000
-0.90	0.0000	0.0000	0.0000	0.0000	0.0000	0.0000
-0.95	0.0000	0.0000	0.0000	0.0000	0.0000	0.0000
-1.00	0.0000	0.0000	0.0000	0.0000	0.0000	0.0000
-1.05	0.0000	0.0000	0.0000	0.0000	0.0000	0.0000

Table S7.

The average surface tension of solid and liquid Au at different chemical potentials of CO, $\mu_{CO}(T, P)$. And the corresponding melting point of Au NPs with radius r at 1, 2, 3, and 4 nm.

$\mu_{CO}(T, P)$	γ_l (J/m^2)	γ_s (J/m^2)	T_m (K) (r =1 nm)	T_m (K) (r =2 nm)	T_m (K) (r =3 nm)	T_m (K) (r =4 nm)
0.00	-1.2808	1.0781	-	-	-	-
-0.05	-1.0149	1.1327	-	-	-	-
-0.10	-0.7650	1.1821	-	-	-	-
-0.15	-0.5295	1.2243	-	-	-	-
-0.20	-0.3100	1.2608	-	-	-	-181.65
-0.25	-0.1066	1.2904	-	-	-	-1.36
-0.30	0.0825	1.3141	-	-	-219.40	169.70
-0.35	0.2555	1.3308	-	-	-4.23	331.08
-0.40	0.4125	1.3441	-	-	193.39	479.29
-0.45	0.5535	1.3548	-	-109.89	372.41	613.56
-0.50	0.6800	1.3632	-	133.49	534.66	735.25
-0.55	0.7922	1.3690	-	352.19	680.46	844.60
-0.60	0.8867	1.3726	-258.75	539.13	805.08	938.06
-0.65	0.9668	1.3744	62.71	699.86	912.24	1018.43
-0.70	1.0309	1.3748	323.55	830.28	999.18	1083.64
-0.75	1.0805	1.3750	526.50	931.75	1066.83	1134.37
-0.80	1.1142	1.3750	664.38	1000.69	1112.79	1168.85
-0.85	1.1318	1.3750	736.61	1036.81	1136.87	1186.90
-0.90	1.1350	1.3750	749.74	1043.37	1141.25	1190.19
-0.95	1.1350	1.3750	749.74	1043.37	1141.25	1190.19
-1.00	1.1350	1.3750	749.74	1043.37	1141.25	1190.19
-1.05	1.1350	1.3750	749.74	1043.37	1141.25	1190.19

Table S8.

Reaction energies (ΔE) and barriers (E_a) of each step for the dissociative L-H and associative L-H pathways on Au(111), Au(100), Au(211), Au(221), Au(311), and Au(321) surfaces based on DFT calculations.

	Reactions	ΔE	E_a
Au(111)	* + CO(g) → *CO	-0.25	
	* + O_2(g) → *O_2	-0.02	
	* + *O_2 → 2*O	0.33	1.97
	*CO + *O → 2* + CO_2(g)	-3.08	0.13
	CO + O_2 → *COOO + *	-0.45	0.12
	*COOO → *O + CO_2(g)	-2.29	0.22
Au(100)	* + CO(g) → *CO	-0.44	
	* + O_2(g) → *O_2	-0.04	
	* + *O_2 → 2*O	-0.16	1.00
	*CO + *O → 2* + CO_2(g)	-2.61	0.03
	CO + O_2 → *COOO + *	-0.50	0.12
	*COOO → *O + CO_2(g)	-2.27	0.13
Au(211)	* + CO(g) → *CO	-0.62	
	* + O_2(g) → *O_2	-0.21	
	* + *O_2 → 2*O	-0.15	1.61
	*CO + *O → 2* + CO_2(g)	-2.39	0.31
	CO + O_2 → *COOO + *	-0.24	0.78
	*COOO → *O + CO_2(g)	-2.30	0.21
Au(221)	* + CO(g) → *CO	-0.70	
	* + O_2(g) → *O_2	-0.15	
	* + *O_2 → 2*O	0.36	1.49
	*CO + *O → 2* + CO_2(g)	-2.62	0.11
	CO + O_2 → *COOO + *	-0.17	0.16
	*COOO → *O + CO_2(g)	-2.09	0.50
Au(311)	* + CO(g) → *CO	-0.64	
	* + O_2(g) → *O_2	-0.12	
	* + *O_2 → 2*O	-0.14	1.37
	*CO + *O → 2* + CO_2(g)	-2.52	0.93
	CO + O_2 → *COOO + *	-0.31	0.77
	*COOO → *O + CO_2(g)	-2.35	0.19
Au(321)	* + CO(g) → *CO	-0.80	
	* + O_2(g) → *O_2	-0.03	
	* + *O_2 → 2*O	0.04	1.22
	*CO + *O → 2* + CO_2(g)	-2.52	0.63
	CO + O_2 → *COOO + *	-0.18	0.13
	*COOO → *O + CO_2(g)	-2.30	0.10

Table S9.

Reaction energies (ΔE) and barriers (E_a) of each step for the dissociative L-H and associative L-H pathways on the Au site of multi-layer $Au_{12}/CeO_2(111)$ based on DFT calculations.

	Reactions	ΔE	E_a
$Au_{12}/CeO_2(111)$	$* + CO(g) \rightarrow *CO$	-0.74	
	$* + O_2(g) \rightarrow *O_2$	-0.38	
	$* + *O_2 \rightarrow 2*O$	-0.31	2.11
	$*CO + *O \rightarrow 2* + CO_2(g)$	-1.81	0.46
	$*CO + O_2* \rightarrow *COOO + *$	-0.20	0.28
	$*COOO \rightarrow *O + CO_2(g)$	-2.30	0.45

Table S10.

Reaction energies (ΔE) and barriers (E_a) for the M-vK pathways at the interface site of $Au_{12}/CeO_2(111)$ based on DFT calculations.

	Reactions	ΔE	E_a
$Au_{12}/CeO_2(111)$ Interface	$* + CO(g) \rightarrow *CO$	-0.74	
	$*CO + {}^{\#}O \rightarrow *COO^{\#}$	-0.88	0.11
	$*COO^{\#} \rightarrow * + {}^{\#}(Ov) + CO_2(g)$	1.48	
	${}^{\#}(Ov) + O_2(g) \rightarrow {}^{\#}O_2$	-2.62	
	${}^{\#}O_2 + * + CO(g) \rightarrow {}^{\#}O_2 + *CO$	-0.92	
	$*CO + {}^{\#}O_2 \rightarrow *COOO^{\#}$	-0.24	0.20
	$*COOO^{\#} \rightarrow * + {}^{\#}O + CO_2(g)$	-2.60	0.26

Table S11.

The diameter (*d*) and the number of atoms on the exposed solid Au surfaces and interface atoms on Au/CeO_2 on supported Au NP of Au_{37}, Au_{155}, Au_{260}, Au_{476}, Au_{756}, Au_{1001}, Au_{1659}, Au_{3382} and Au_{7439} NPs.

NPs	*d*/nm	Exposed solid Au surfaces						Interface
		(100)	(111)	(211)	(221)	(311)	(321)	
Au_{37}	1.2	3	0	0	0	9	0	12
Au_{155}	1.7	3	34	9	12	0	12	18
Au_{260}	2.3	3	63	12	15	0	12	24
Au_{476}	2.9	3	120	12	27	0	12	30
Au_{756}	3.5	12	169	24	27	0	12	36
Au_{1001}	4.0	12	222	24	45	0	12	42
Au_{1659}	4.6	27	327	36	39	0	12	48
Au_{3382}	5.8	3	402	48	129	12	48	66
Au_{7439}	7.5	27	972	60	51	60	60	78

Table S12.

The number of different coordinated Au atoms (0~9) and liquid-like atoms on the supported Au_{37}, Au_{155}, Au_{260}, Au_{476}, Au_{756}, Au_{1001}, Au_{1659}, Au_{3382} and Au_{7439} NPs.

NPs	0	1	2	3	4	5	6	7	8	9	Exposed Au liquid
Au_{37}	0	0	0	0	0	3	0	9	3	0	15
Au_{155}	0	0	0	0	0	0	12	21	3	34	70
Au_{260}	0	0	0	0	0	0	12	27	3	63	105
Au_{476}	0	0	0	0	0	0	12	39	3	120	174
Au_{756}	0	0	0	0	0	0	12	51	12	169	244
Au_{1001}	0	0	0	0	0	0	12	57	12	222	303
Au_{1659}	0	0	0	0	0	0	12	75	27	327	441
Au_{3382}	0	0	0	0	0	0	48	189	3	402	642
Au_{7439}	0	0	0	0	0	0	60	171	27	972	1230

Movie S1.
DPMD trajectories showing $Au_{61}/CeO_{2-x}(111)$ without CO at 475 K.

Movie S2.
DPMD trajectories showing $Au_{61}/CeO_{2-x}(111)$ with CO at 475 K.

Movie S3.
DPMD trajectories showing $Au_{287}/CeO_{2-x}(111)$ without CO at 675 K.

Movie S4.
DPMD trajectories showing $Au_{287}/CeO_{2-x}(111)$ with CO at 675 K.

Movie S5.
DPMD trajectories showing $Au_{576}/CeO_{2-x}(111)$ without CO at 675 K.

Movie S6.
DPMD trajectories showing $Au_{576}/CeO_{2-x}(111)$ with CO at 675 K.

Movie S7.
DPMD trajectories showing $Au_{2791}/CeO_{2-x}(111)$ without CO at 800 K.

Movie S8.
DPMD trajectories showing $Au_{2791}/CeO_{2-x}(111)$ with CO at 800 K.

Data S1. (Data S1.xlsx as a separate file)

The detailed data of calculated surface energies for solid Au(*hkl*) (*h*, *k*, and $l < 3$) surfaces.

Data S2. (Data S2.xlsx as a separate file)

The data of unit surface area (A_i) and averaged CO adsorption energies on solid Au(*hkl*) (*h*, *k*, and $l < 3$) surfaces and liquid Au surface with coverages of 1/4, 1/2, 3/4, and 1.

Data S3. (Data S3.xlsx as a separate file)

The data of melting temperature (T_m) of Au NPs with different sizes.

Data S4. (Data S4.xlsx as a separate file)

The data of calculated TOF from microkinetic modeling of Au(100), Au(211), Au(311), Au(221), Au (111), Au_{12}/CeO_2 interface, and Au site on Au_{12}/CeO_2 at range of temperatures from 200 to 600 K and the total pressure of 1 bar.

Data S5. (Data S5.xlsx as a separate file)

The data of Statistical TOF of supported Au_{7439}, Au_{3382}, Au_{1659}, Au_{1001}, Au_{756}, Au_{476}, Au_{260}, Au_{155}, Au_{37}, and Au_{12} NPs on CeO_2(111).